TECHNISCHE UNIVERSITÄT WIEN

DIPLOMARBEIT

Exploring field-induced remnant magnetization traps for ultracold atoms on a niobium atomchip

ausgeführt am Atominstitute

ATOMINSTITUT

der Technische Universität Wien
Fakultät für Physik

unter der Anleitung von
Univ.Prof. Dipl.-Ing. Dr.techn. Hannes-Jörg Schmiedmayer
und
Projektass. Dr.rer.nat Fritz Diorico MSc.
Projektass. Dr.techn. Dipl.-Ing. Stefan Minniberger

durch

Naz Shokrani

Matrikelnummer: 01228608

Abstract

Atomchips serve as versatile quantum optics devices to manipulate ultracold atoms. Having a superconducting (SC) atomchip not only provides us with a long coherence time for future hybrid quantum systems, but also gives the opportunity to investigate properties of SC materials. In this work, the niobium Z-structure of an atomchip is magnetized by an external magnetic field pulse. The hysteresis behaviour of the type-II SC structure is then used to trap the atoms without applying a chip current and the influence of this magnetization on the trapping the atoms is probed. More characteristics of the field-induced remnant magnetization trap are checked, like trap-stability and the distance of the atom cloud to the trapping wire for different bias fields.

Zusammmmmenfassung

Atomchips sind nützliche Werkzeuge in der Quantenoptik um ultrakalte Atome zu manipulieren. Ein supraleitender Atomchip sorgt nicht nur für lange Kohärenzzeiten wie sie für zukünftige hybride Quantum systeme benötigt werden, sondern eröffnet auch die Möglichkeit Eigenschaften des Supraleiters zu untersuchen. In dieser Arbeit, die Niobium Z-Struktur unseres Atomchips wird durch einen externen Magnetfeldpuls magnetisiert. Das hysteretische Verhalten dieses Typ-II Supraleiters wird dann verwendet, um Atomwolken ohne Anlegen eines Stromes an den Atomchip zu fangen. Weitere Details der feldinduzierten remanenten Magnetisierung, wie die Stabilität der Falle oder der Abstand der Falle von der Chipoberfläche in Abhängigkeit des äußeren Fallenfeldes werden untersucht.

Table of contents

Part I

Preliminaries

Chapter 1

Introduction

Ultracold atom physics paves the way for investigation of new aspects of the fascinating world of quantum physics. The behavior of an ultracold system can be determined solely by the quantum statistical nature of the gas particles and their interaction. Since the late 1980s physicists used laser to cool and collect small clouds of atoms to temperature below milli Kelvin. Thank to ultracold atom processes, a new state of matters was finally observed, applying cooling methods like laser- and evaporative cooling coming along with trapping of atoms. It was more than 70 years after the theoretical prediction of this state by A. Einstein and S. Bose, that a temperature drop below the critical temperature for Bose- Einstein condensate (BEC) could be achieved. Some of the first pioneers of the realization of BEC were awarded the Nobel prize in 1997 [1].

Ultracold atoms can be manipulated, trapped or cooled either by light and, or magnetic fields. One possibility to have versatile robust magnetic traps is to use an "atomchip". These micro devices mounted on surfaces provide us with miniaturized electric and magnetic potentials and guides for atoms at a scale of less than one micrometer [2]. Atomchips enable controlled quantum manipulation of ultracold atoms. With lithography and other processes, complex surface structures can be fabricated to provide various tight trapping potentials for cold atoms in the proximity of the microchip surface. Atomchips consist of normal conducting as well as superconducting current-carrying wires.

Superconductivity is a distinctive property of special materials that exhibits zero resistance and expel magnetic flux from their interior below a certain critical temperature for specific external magnetic fields. The zero-resistivity implies zero heat dissipation for a transport current. This property makes the superconductors an appealing candidate for the experiments sensitive to thermal noise to provide the possibility of reduction of the Johnson-Nyquist noise. As the fluctuations of electromagnetic fields originated from metallic surfaces can lead to loss and decoherence of trapped atoms which limits the performance of the atomchip,

superconducting atomchips were implemented in recent years. Superconducting atomchips have been shown to reduce both the near field noise and technical noise compared to their normal conducting counterparts [3]. The spin-flip lifetime and coherence of the trapped atoms improves accordingly.

The primarily goal of this experiment has been the creation of a hybrid quantum systems, where an ensemble of ultracold atoms is strongly coupled to the near field of a superconducting waveguide coplanar resonator. In [4] it has been shown that one can achieve strong coupling with currently available technology of circuit cavity quantum electrodynamics and ultracold atomic ensembles on an atomchip. The strong coupling between a single microwave photon in the waveguide resonator and a collective hyperfine qubit state in the ensemble can be used to study and control atomic motion or to cool the resonator field via the atoms.

Studying the behavior of type-II superconductor traps has been another target of this experiment. The particular interest in this work is investigating the effect of field magnetization of a type-II superconducting atomchip on trapping the atoms. A special type of trap has been experimentally demonstrated without applying any transport current. The superconducting Nb Z- structure is magnetized by an external magnetic pulse perpendicular to the chip surface. The so called remnant magnetization trap is here purely field-induced. In contrast, the current-induced magnetization hysteresis defines a different type of atom trap which is discussed comprehensively in [5]. For high temperature superconducting atomchip consisting of YBCO, the field- and current induced magnetization traps are investigated and discussed in [6–8]. One characteristic of the mixed state of a type II superconductor is the presence of vortices. The vortices affect the trapping potentials generated by magnetized superconducting structures in the mixed state. The properties of these vortex-based traps depend directly on the vortex distribution. This also implies that sufficiently cold atoms could be used as a sensitive probe of the distribution and dynamics of vortices in superconductors, as discussed for a YBCO atomchip in [6]. In this process the near-field noise is significantly reduced and technical noise decreases as the transport current is absent. Thus, the main goal of this thesis is to investigate the remnant magnetization trapping abilities of niobium for potential atom trapping without the need of external connection for hybrid quantum devices.

This thesis is organized as follows. After this chapter, a brief theory of ultracold rubidium atoms and superconductors is included in chapter 2. Chapters 3 and 4 contain the setup and the operation of the experiment. The following chapter shows the endeavors on the way of achieving BEC on a superconducting atomchip. In the last chapter, a detailed discussion is provided about observation of remnant magnetization trap and its properties. The stability of the trap has been checked during very long scans and the result of all distance measurements are summarized at the end.

Chapter 2

A brief theory of ultracold rubidium atoms and superconductors

2.1 Ultracold Rubidium atoms

Rubidium, the element in the fifth row of alkali metals with atomic number 37 is one of the favorite species to work with in quantum optics and ultracold physics with dilute gases. It has 32 isotopes and can be found in the nature as 72 % of ^{85}Rb with 48 neutrons and 28% ^{87}Rb with 50 neutrons. Despite the higher abundance of ^{85}Rb, these experiments are preferably done with ^{87}Rb due to the positive scattering length[1]. The availability of cheap laser diodes at the correct wavelength, typically used in CD-ROM drives, is another advantage of ^{87}Rb.

From the different transitions in ^{87}Rb, the "D_2" line ($5^2S_{1/2} \rightarrow 5^2P_{3/2}$ pictured in fig. 3.1), is the most commonly used one. The "D_2" line has a cycling transition which can be used for cooling and trapping of ^{87}Rb atoms [10].

In order to understand the basics of magnetic field interaction with a neutral atom, the quantum structure of the atoms will be reminded briefly in the following.

In quantum mechanics, the fine structure appears as a coupling between the orbital angular momentum $\mathbf{L}$ of the outer electron and its spin angular momentum $\mathbf{S}$. The total electron angular momentum is then given by

$$\mathbf{J} = \mathbf{L} + \mathbf{S},$$

---

[1] positive scattering length means the atoms behave mutually repulsive at low temperatures. This prevents a collapse of them to a small condensate. ^{87}Rb is also easy to evaporatively cool, with a consistent strong mutual scattering. The half-life of ^{87}Rb is 4.9210^{10} years [9].

and the magnitude of **J** can take the values

$$|L - S| \leq J \leq L + S.$$

For the ground state of ^{87}Rb $L = 0$ and $S = 1/2$, so $J = 1/2$. This state is denoted by $5^2S_{1/2}$ where 5 is the principal number of outer electron, the superscript is $2S + 1$, the letter (S) indicates the orbital name for the angular momentum $L = 1$ and the superscript is J. The first excited state concerns $L = 2$ and consists of $5^2P_{1/2}$ and $5^2P_{3/2}$.

The hyperfine structure on the other hand, is the consequence of the coupling of **J** with the total nuclear angular momentum **I**. The total atomic angular momentum **F** is then given by

$$\mathbf{F} = \mathbf{J} + \mathbf{I},$$

and the magnitude of **F** can take the values

$$|J - I| \leq F \leq J + I.$$

Now the interaction of neutral atoms with an external magnetic field can be described upon these structures as:

$$H_B = \frac{\mu_B}{\hbar}(g_s S + g_L L + g_I I) \cdot \mathbf{B}_{ext},$$

where g refers to the different g-factors and $\mu_B = e\hbar/2m_e$ is the **Bohr magneton**. If J and F are good quantum numbers with the meaning that the energy splitting is small compared to fine and hyperfine splitting, the interaction becomes:

$$H_B = \mu_B \, g_F \, F_z \, B_z. \tag{2.1}$$

Here the magnetic field is considered to be along the z-direction (i.e., along the atomic quantization axis) and g_F refers to the **hyperfine Landé g-factor**.

2.1.1 Laser cooling, Doppler limit and beyond

Laser cooling relies on the force the light can exert on atoms. The optical force has two components, the dipole force which can be used for trapping, and the radiative force, also called scattering force [11] for cooling of atoms. The frequency difference δ between a laser beam and the atomic transition is called detuning. It is negative when the laser is red detuned or positive for blue detuned light. The absorption cross section of an atom depends

on the detuning, it will be maximum at zero detuning. Due to the well known **Doppler effect** [12], the resonance frequency of atoms moving towards a laser beam is shifted to lower frequencies, while atoms moving away have an apparent higher resonance frequency. When shinning a **red detuned** laser beam in a dilute atomic gas, the atoms moving towards the beam are closer to resonance than the atoms moving away from the beam. Therefore, the absorption becomes velocity dependent: atoms moving towards the beam are more likely to absorb a photon. The subsequent re-emission of photons happens in a random direction. Over many scattering events, the emissions average to a net momentum of zero, while the absorption of photons from the laser beam slows the atoms down [13]. The re-emitted photons have a slightly higher frequency (and energy) than the absorbed ones. This energy difference is removing the kinetic energy and thus cooling the gas. This describes how atoms get slowed down in one direction. In order to actually cool a gas, 6 counterpropagating beams in all three perpendicular directions are required. This cooling process is called Doppler cooling which plays an essential role in laser cooling [1]. Doppler cooling has a limit which comes from the fact that in this process the atoms get heated as well due to the random nature of spontaneous emission [14]. The competing laser cooling and diffusion heating processes reach an optimum when $\delta = \Gamma/2$, where Γ is the decay rate. The temperature limit is the Doppler temperature:

$$T_D = \frac{\hbar\Gamma}{2k_B} \, ,$$

where k_B is the Boltzmann constant. For rubidium atoms with a decay rate of around 18 MHz the Doppler temperature is approximately 144 μK.

However temperatures much lower than T_D were measured while laser cooling an atomic sample. To explain this sub-Doppler cooling, polarization of the beam should be considered. Two configurations can provide the polarization gradient for this cooling:

I) lin $\perp$ lin configuration

In this configuration two counter propagating beams are applied with linear polarization perpendicular to each other. Their interference results in a standing wave with polarizations σ_+, linear and σ_- in a half wave length as fig. 2.1a shows. This causes a sinusoidal **light shift** in the ground state. The light shifts of the different sublevels change with polarization which comes from the different Clebsch-Gordan coefficients showing the strength of atom-light field coupling, as discussed in [13, 14]. So the polarization and therefor the sublevels of the atom is position dependent. Optical pumping causes a larger population in the state where the light shift is larger. When the light field is σ_+, the (negative) light shift of $m_g = 1/2$ is

three times than the light shift of the sublevel $m_g = -1/2$. Due to this reason where the light field is σ_+, optical pumping brings the atoms to the sublevel of $m_g = 1/2$ ground state from $m_g = -1/2$ and σ_- brings them to the ground state with sublevel $m_g = -1/2$. Sinusoidal variation of the ground-state sublevels is depicted in fig. 2.1b, showing where each m_g has maximum or minimum of the energy.

As the atom moves, it climbs the potential hill of the specific m_g state, but as it nears the top of the hill the polarization of the light changes and an optical pumping occurs. The atom is now again at the bottom of a hill, and it again must climb, losing kinetic energy, as it moves. In summary, by climbing of potential hill kinetic energy changes to potential energy and optical pumping (discussed in sec. 2.1.2) leads to spontaneous emission and some energy is radiated away as spontaneous emission happens at higher frequency than the absorption. The two procedures of (distinctive) light shift and optical pumping play the crucial roles in this cooling process. The nonadiabatic motion of climbing of the potential hills and the following optical pumping which brings the atomic population on the lowest energy level reminds the Greek myth of Sisyphus. Therefrom, the procedure is called **Sisyphus cooling**.
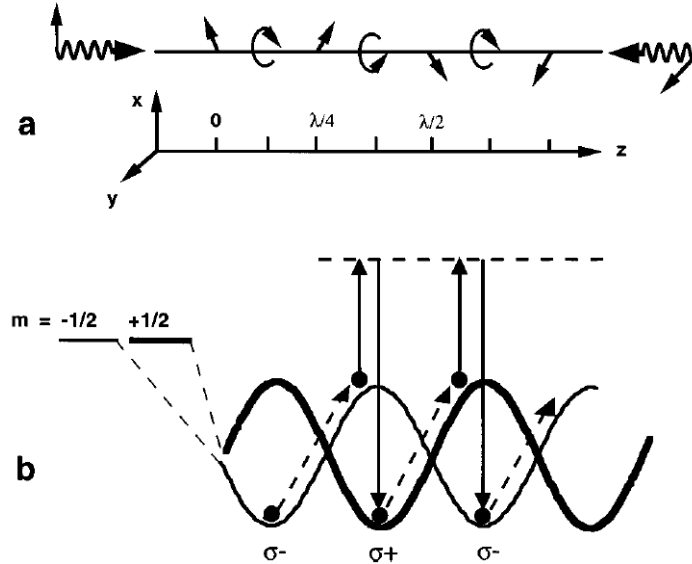
Fig. 2.1 The Spatial configuration of a lin $\perp$ lin polarization gradient. a) Shows the polarization gradient used for cooling. b) The ground state sublevels of $J = 1/2 \Leftrightarrow 3/2$ transition are shifted differently in the light field. Continuous arrows show optical pumping which bring atoms to the lowest energy level. The absorbed light in the optical pumping has a lower frequency than the emitted one, therefor energy dissipates to the radiation field. Picture taken from [13].

II) $\sigma_+ - \sigma_-$ configuration

In contrast to the previous configuration, two counter propagating σ_+ and σ_- polarized beams result in a standing wave with linear polarization whose direction rotates in position. The atoms at rest can absorb from two beams with the same probability and there is no net force on them. These atoms occupy mainly the $m_F = 0$ substate. Their quantization axis follows the local polarization and the absorption from two beams is the same since a linear polarization can be considered as half σ_+ - and half σ_- polarization. The atoms even with a very low velocity have an orientation with respect to the local polarization. Their quantization axis can not follow the local polarization direction adiabatically. So they can not stay at $m_F = 0$ substate. In [14] it is shown, that atoms moving towards the laser beam with σ_+ (σ_-) polarization are preferentially occupying the $m_F = +1$ ($m_F = -1$) substate. Atoms with $m_F \neq 0$ have a preference towards σ_+ or σ_- absorption due to Clebsch–Gordan coefficients. The preferential absorption and scattering of the opposing laser beam leads to a radiation pressure which can effectively cool the atoms.

Both configurations lead to a net frictional force and slow down the atoms. The slowing force is velocity dependent as if atoms moves in a thick and sticky medium so the cooling method beyond Doppler limit is called optical molasses.

The limit for these cooling techniques is the recoil generated by the emission of a single photon. The temperature limit becomes $T_R = \frac{\hbar^2 k^2}{2M k_B}$, which is for rubidium atoms around $0.7\,\mu\text{K}$.

The configuration used in this work for cooling in the molasses is the $\sigma_+ - \sigma_-$ configuration. As we will see in the following section, this configuration is also required for the MOT. The difference between MOT and molasses is then the detuning.

2.1.2 Magneto Optical Trapping

The radiation pressure can be used to cool the atoms to very low temperatures but is not enough to trap the atoms. We still need a restoring force to keep them in the trap region. The most common trap for neutral atoms utilizes both magnetic and optical fields producing a magneto-optical trap (MOT). The MOT is based on an inhomogeneous magnetic field achievable with simple coils and the radiation pressure created by six counterpropagating laser beams in three orthogonal directions. The coils generate a magnetic quadrupole field, with zero magnetic field in the trap center. The magnetic field causes a position dependent splitting of the Zeeman sublevels. In the fig. 2.2 the center (z=0) corresponds to B=0. Away from the center, the field increases linearly with distance. On positive side of the z-axis, Zeeman splitting shifts the sublevel $+1$ up- and the -1 level downwards and the opposite

holds for these levels on the negative side of the axis. Two opposing laser beams are used with the same intensity and frequency, with some red detuning . Their polarization is circular and clockwise with respect to the direction of propagation. The two beams are equally absorbed from the atoms in the center and there is no net radiation force on the atoms there. The atoms on the right (left) side with $m_F = -1$ ($m_F = +1$) however, are closer to resonance with the σ_- (σ_+) beam coming from right (left) and can absorb photons from this beam more likely than from the σ_+ (σ_-) beam. Therefore atoms experience a net force towards the center. We now have position dependent force towards the trap center.

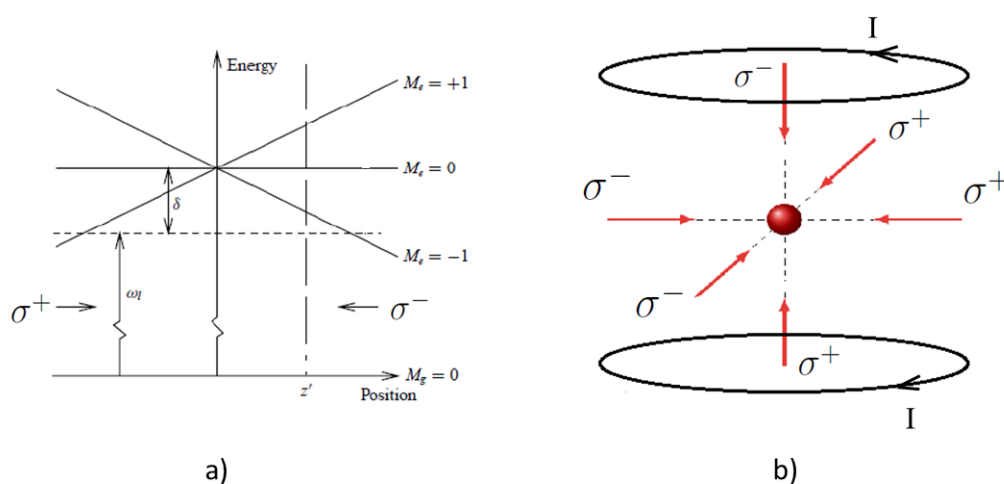a)   b)

Fig. 2.2 Spatial configuration of MOT. a) Energy levels of a hypothetical atom with ground state $J = 0$ and excited state $J = 1$. The Zeeman splitting of the excited state is denoted with $M_e = -1, 0, +1$ here. The dashed line shows the frequency of two laser beams. The σ_- beam coming from right couples the ground state $M_g = 0$ with the $M_e = +1$. Due to the Zeeman splitting of the levels and with the detuning δ, atoms at $z = z'$ are closer to resonance with the σ_- beam. b) Trapping scheme in three dimensions.

Repumping and Optical pumping

Although the ^{87}Rb has an almost closed cooling cycle of $|F = 2\rangle \rightarrow |F' = 3\rangle$ which is used for cooling and imaging, some of the atoms can decay to the ground state $|F = 1\rangle$ and fall out of the cooling cycle. A repumper laser resonant with $|F = 1\rangle \rightarrow |F' = 2\rangle$ brings these atoms back and lets the cooling proceed.

In Sec. 2.1.1 we discussed how optical pumping is used in the (Sisyphus) cooling. Optical pumping induce a transition from $F = 2$ to $F' = 2$. It is typically done with the aid of a σ_+ beam from the substate m_F in $F = 2$ to the substate $m_{F'+1}$ in $F' = 2$. Consequently the atoms will go up the m_F ladder, ending in $m_F = +2$ substate.

2.1.3 Magnetic trapping

There is an interaction between the magnetic moment of the atom $\vec{\mu} = g_F \mu_B \vec{F}$ and an inhomogeneous magnetic field,

$$\vec{F}_{mag} = \vec{\nabla}(\vec{\mu} \cdot \vec{B}) . \tag{2.2}$$

This interaction can be used to trap neutral atoms magnetically. The corresponding potential can be written as,

$$V_{mag} = - \vec{\mu} \cdot \vec{B} . \tag{2.3}$$

As this interaction depends on the angle between the magnetic field direction and the moment of the atoms, the orientation of $\vec{\mu}$ in the field should be preserved. It means only with the the the adiabatic following condition where Larmor precession rate $\omega_z = \mu B / \hbar$ is much larger than the changes of the field orientation in time, this interaction can be described as above. In this case $\vec{\mu}$ follows the direction of $\vec{B}$ and m_F is the constant of the motion.

The atoms with magnetic moments parallel to the field direction have according to eq. (2.3), $V_{mag} < 0$. These atoms are high-field seeking since the minimum of the potential is at the maximum of the field. However the maximum of the field is forbidden where no source exists for the field, according to Maxwell's equations. The low-field seeking atoms (with magnetic moment in the opposite direction of the magnetic field) for which $V_{mag} > 0$ and therefore, $g_F m_F > 0$ are needed for magnetic trapping. The minimum of the magnetic field corresponds to the potential minimum and since Maxwell's equations and therefore Earnshaw's theorem allows the minimum of the field, atoms can be trapped where their potential gets minimum. From the F = 2 ground state of ^{87}Rb with $g_F = 1/2$, the substate $|F = 2 , m_F = 2\rangle$ can be used for magnetic trapping. It fulfills the $g_F m_F > 0$ condition and has also the maximum of the m_F which is necessary to keep the atoms tightly trapped.

2.1.4 Diverse types of magnetic traps

Quadrupole magnetic trap

One of the simplest possible magnetic traps is the quadrupole magnetic trap (QMT). Two coils carrying opposite currents (anti-Helmholtz configuration) construct this trap. This configuration cause a linear trapping potential and builds a single trap where the minimum of the field is zero. Quadrupole traps can be used to transport atom clouds. The transport can be done in two different ways.

- Moving coils

- Transfer from coil to coil

The latter one is used in this experiment. More discussion is in sec. (3.2) and in [15].

Majorana loss: All magnetostatic traps can only trap atoms in their low field seeking states. One of the limitations of the QMT is the Majorana loss. Atoms crossing the zero field region in the trap center experience a sudden change in quantization axis and cannot follow that change adiabatically. This causes a spin flip to an untrapped state and the atoms fall out of the trap.
There are different ways to overcome this limitation like using a plugged QMT where a blue detuned laser beam is applied or a hybrid QMT with an optical dipole trap. The Ioffe-Pritchard type magnetic trap used in this experiment, is one of the proper magnetic trap for this aim.

Ioffe-Pritchard trap

An Ioffe-Pritchard trap (or just Ioffe trap) can be used where a non vanishing minimum of the magnetic field is required. This type of trap prepares a harmonic potential with magnetic field offset and hence it reduces Majorana losses. Many different coils-configurations can lead to a Ioffe trap. Some special configurations of the Ioffe trap are named below;

- cloverleaf configuration which has the advantage of a good optical access.

- baseball configuration having the benefit of less heat dissipation.

- two-dimensional quadrupole field: a trap consisting of four straight currents which form a linear quadrupole field and two end coils. The coils are used for the Longitudinal confinement and have Helmholtz configuration.

- quadrupole-Ioffe trap (QUIC)

QUIC trap

This trap consists of two identical quadrupole coils and one typically smaller Ioffe coil. The Ioffe coil is mounted between the two quadrupole coils and perpendicular to them. Currents flowing through the quadrupole coils or the Ioffe coil can be adjusted independently to build a quadrupole- or a QUIC trap. There is no need of extra compensation coils for this trap.

Atomchips

An elaborate quantum optics device to manipulate cold atom is the "atomchip". There are micro-structures miniaturized and mounted on a chip which integrates matter wave optics [2]. Atomchip equips us with more robust and much smaller facilities for a magnetic trap. They also provide much easier heat dissipation which allow higher current density to be sent through the wires. Common substrates used in atomchips with good heat conduction are Si, GaAS and Sapphire. The distinguishable characteristic of the atomchips is the possible magnetic field GRADIENT. With strong bias fields, atomchips allow for tighter confinement of atoms in the traps. The magnetic field of a long current carrying wire is given by $B(r) = \frac{\mu_0 I}{2\pi r}$. So the field gradient changes with the square of the distance as can be deduced from the derivative: $\frac{dB(r)}{dr} = \frac{\mu_0 I}{2\pi r^2}$. Wires with length of mms and thickness of μms are designed for an atomchip in the way that they build simple guides for the cold atoms and then the trapping potential is closed with bending the current-carrying wire. The two main kinds of traps built by the miniaturized wires are:

- U-traps: the magnetic field vanishes completely at the trap minimum.

- Z-traps: a vanishing magnetic field can be avoided by bending the wire ends to form a"Z". This configuration creates an Ioffe type trap. See fig. 2.3.
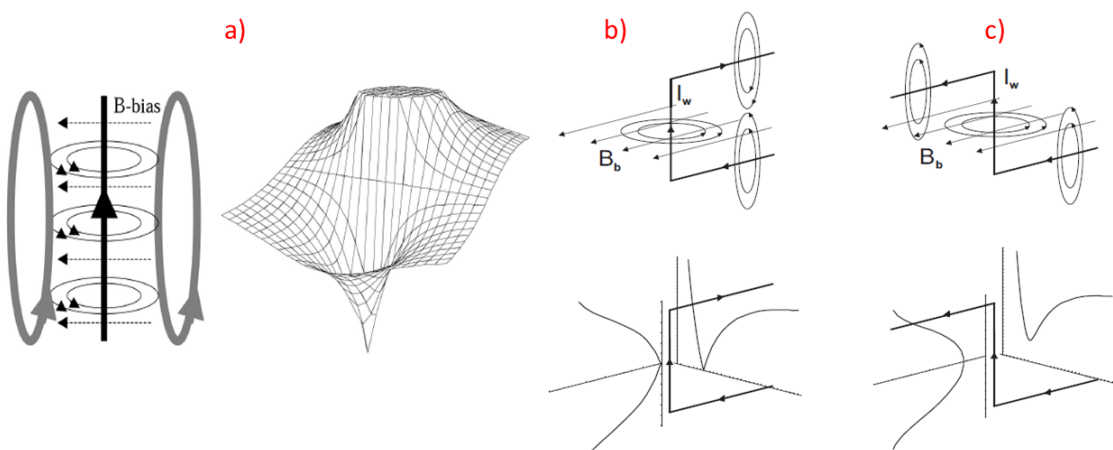

Fig. 2.3 Trap schemes including a current carrying wire. a) A simple trap consisting of a magnetic quadrupole field plus a constant bias field to trap atoms in low field seeking states and the corresponding potentials. b) and c) bent-wire traps: U- and Z-traps. Pictures from[2].

2.1.5 Phase space density

Laser cooling not only leads to low temperature samples of atoms but also can increases the density of the sample. The phase space density (PSD), denoted by $D(\vec{r}, \vec{p}, t)$ is the probability of finding the particle at a particular position and time with the momentum $\vec{p}$. For a gas of cold atoms, it is defined as $D = n\lambda_{dB}{}^3$, where λ_{dB} is the deBroglie wavelength: $\lambda_{dB} = \frac{h}{\sqrt{2\pi m k_B T}}$. In a QMT, the density of the gas (n) is: $n = \frac{N}{4\pi}\left(\frac{\mu\alpha}{k_B T}\right)^3$, where α, μ depend on the magnetic trap and atoms inside. Hence, the PSD for a magnetic trap becomes:

$$D \propto \frac{N}{T^3}.$$

The PSD can not be increased on and on. The increase of the PSD reaches its limit when increasing the density induces an increase in collision rate and so it causes an enhanced loss of cold atoms. Reaching higher PSD is of great importance since high enough PSD origins a phase transition. For the specific value of PSD, $D \cong 2.612$, a cold gas of atoms undergoes a phase transition called **Bose-Einstein Condensate** (BEC). The prediction of this phase transition stated first Bose and Einstein in 1920s. A BEC starts to form when all bosonic particles of an ultra cold gas accommodate in their (lowest possible) ground state. In this state, the thermal de-Broglie wavelength becomes comparable with the interatomic distance and the individual wavefunctions start to overlap. W. Ketterle, E. Cornell and C. Wieman produced the first gaseous condensate in 1995.

2.1.6 Evaporative cooling

In the last step of cooling and trapping atoms, where optical and magnetic fields can not cool the atoms further, "evaporative cooling" comes in.

By this procedure, high-energy trapped atoms are removed continuously from the trap. The evaporated atoms carry away more than average energy and the remaining atoms rethermalize. These processes result in a considerable reduction of the temperature of the residual cloud. Evaporative cooling can be performed by a radio-frequency (RF) or a microwave (mw). The radiation flips the atomic state so that the atoms are not in low seeking states and can not be trapped. This method is energy selective, atoms with specific energy can be addressed. Other atoms rethermalize. In this way there is no need to change the trapping potential to lower the depth.
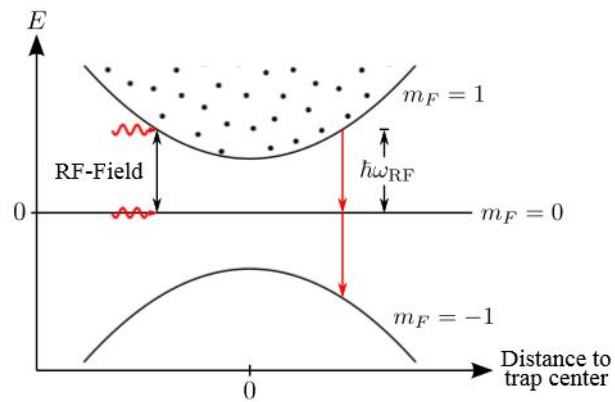
Fig. 2.4 Evaporative cooling in a magnetic trap. The hotter atoms can be addressed by this cooling method in the way that their m_F states change to untrapped states and they can fall off the trap. In consequence the temperature of remaining atoms decrease. Figure is taken from [16].

2.2   Superconductors

The first traces of superconductivity were observed by Kamerlingh Onnes in 1911, when he saw zero electrical resistance while cooling mercury to very low temperatures [17]. He was the first one who could liquefy helium and reach such low temperature that he was able to observe the sudden drop of mercury's resistance at 4.2 K [18]. Before the discovery of Onnes, the behavior of the resistance at very low temperatures was unknown [18]. A brief history of superconductivity will be presented here, following the refs. [19, 20].

In 1933 W. Meissner and R. Ochsenfeld observed expulsion of magnetic flux occurring in certain materials when cooling the sample below the characteristic critical temperature T_c. This behavior is called the Meissner effect. The investigation on superconductivity was then followed by London two-fluid model and the prediction of the penetration depth λ. The two fluid refer to normal electrons with density n_n moving like the free electrons in a normal metal where there get hindered by impurities and thermal vibrations of the ion lattice, and second fluid consisting of superconducting electrons with n_s density moving without scattering which gives rise to the zero resistivity. Scattering of the normal electrons leads to a constant current in a constant electric field, whereas the absence of scattering of the electrons in a superconductor means that the current density would increase steadily in a constant electric field and to have a constant current density, the field should be zero so all the currents need to be carried by superconducting electrons. On the other hand, with no electric field within the superconductor, there will be no potential difference across it, and so it has zero resistance [21].

A new behavior of superconductors was observed in the presence of magnetic fields in 1937 by Shubnikov, later called type II superconductors. In order to describe superconductivity, Fritz and Heinz London presented the first phenomenological theory in 1935 which was able to explain the Meissner effect[22]. As the London theory does not take into account quantum effects, the Ginzburg-Landau (GL) theory was introduced in 1950 [23]. The GL theory is based on Landau's theory of second order transitions and describes the differences between type I and type II superconductors. The second order phase transition refers to a transition at which the state of the system is changing continuously, but its symmetry changes abruptly [24].

A microscopic theory of superconductivity was presented in 1957 by Bardeen, Cooper and Schrieffer (BCS theory) which was the first fully quantum mechanical theory to completely describe the microscopic mechanism involved in superconductivity of low-T_c superconductors [18]. Their theory is based on electron-lattice-electron interaction mediated by the phonons [25].
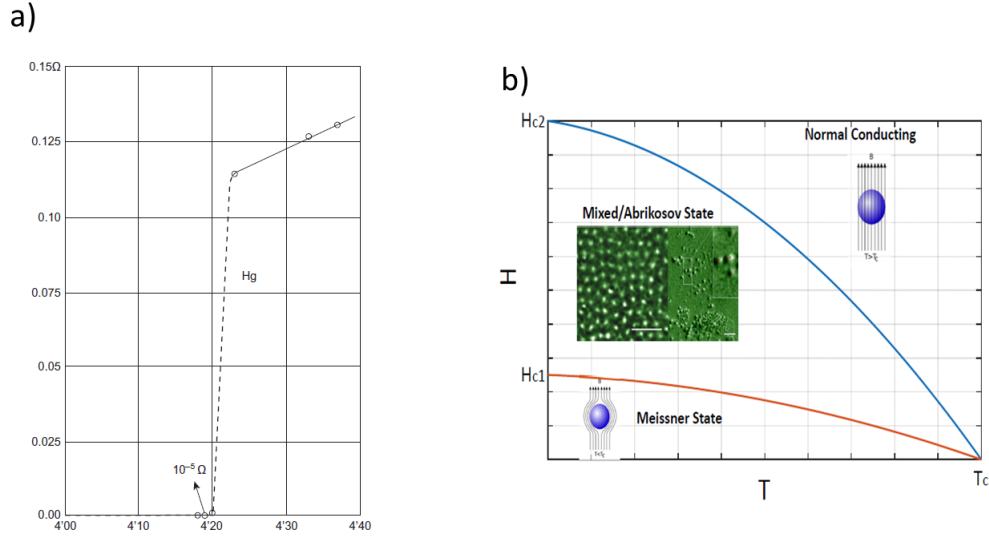
a)

b)

Fig. 2.5 Two specifications of the superconductors: zero electrical resistivity and vanishing magnetic flux. a) the historic graph of dropping the electrical resistivity for Hg around 4.2 K taken from[18]. b) Type II Superconductors. In the Meissner state and for $T < T_c$, magnetic flux can not penetrate into the superconductor. a) taken from [18] and b) from [26] .)

London equations

The first equation of London denotes the fact that current-transport occurs loss-free in a superconductor, with no damping. The equation can be driven from the Ohm's law:

$$\mathbf{j}_s = \sigma_s \mathbf{E} = \left(\frac{n_s e^2 \tau}{m} \right) \mathbf{E}. \tag{2.4}$$

By taking the curl of both sides and using $\nabla \times \mathbf{E} = -\frac{\partial \mathbf{B}}{\partial t}$ we get:

$$\nabla \times \mathbf{j}_s = -\frac{e^2 n_s}{mc} \mathbf{B}, \tag{2.5}$$

where $j_s = n_s e v$ is the superconducting current density, e the elementary charge and n_s the density and m the mass of superconducting charge carriers.

With the Maxwell's equation $\nabla \times \mathbf{B} = \mu_0 \mathbf{J}$ and $\nabla . \vec{B} = 0$, one can easily calculate the second Landon equation,

$$\nabla^2 \mathbf{B} = \frac{1}{\lambda_L^2} \mathbf{B}, \tag{2.6}$$

with the one dimensional solution $B(x) = B_0\, e^{-x/\lambda_L}$, where $\lambda_L = \sqrt{\frac{m}{\mu_0 n_s e^2}}$ is the London penetration depth. According to the second equation of London, the magnetic field decays within a depth of λ_L from the surface of a superconductor which conforms the Meissner effect.

BCS theory

BCS Theory modeled by John Bardeen, Leon Cooper, and Robert Schrieffer, describes the behaviors of type I superconductors. In this theory an electron in the lattice causes a slight increase of the positive charge around it. This increase in positive charge will, in turn, attract another electron. These two electrons are known as a Cooper pair. Consequently an attractive interaction between electrons mediated by phonons can lead to a ground state separated from excited states by an energy gap. The theory describes superconductivity as a microscopic effect caused by a condensation of Cooper pairs into a boson-like state. The current in superconductors is made up of these Cooper pairs, rather than individual electrons. If the energy required to bind these electrons together is less than the energy from the thermal vibrations of the lattice, attempting to break them apart, the pair will remain together. Hence, the thermal vibration of the lattice must be small enough to allow the forming of Cooper pairs.

Ginzburg-Landau theory

Ginzburg and Landau extended the theory of superconductivity by their phenomenological theory via introducing a free energy and a complex order parameter, ψ that defines the state of order of the superconductor.

The order parameter ψ is 0 in the normal state and finite in the superconducting state. The free energy F reads:

$$F = F_{nc} + \alpha|\psi|^2 + \beta|\psi|^4 + \frac{1}{2m}|(-i\hbar + 2e\mathbf{A}\nabla)\psi|^2 + \frac{\mathbf{B}^2}{2\mu_0} \tag{2.7}$$

Minimization with respect to the vector potential A and ψ gives the well-known Ginzburg-Landau (GL) equations [23], i.e.,

$$\mu_0\,\mathbf{J} = \frac{ie\hbar}{2m}(\psi\nabla\psi^* - \psi^*\nabla\psi) + \frac{2e^2}{m}|\psi|^2\mathbf{A}, \tag{2.8}$$

$$0 = \alpha\psi + \beta\psi^3 + \frac{1}{2m}(-i\hbar + 2e\mathbf{A}\nabla)^2\psi. \tag{2.9}$$

If we now set the external field or rather the vector potential $\mathbf{A}$ zero and normalize the order parameter $\psi = \left[\left(\frac{|\alpha|}{\beta} \right)^{1/2} f \right]$ we can deduce from the first GL eq.2.7 the following differential equation,

$$\frac{\hbar^2}{2m|a|} \frac{d^2 f}{dx^2} + f(1 - f^2) = 0. \tag{2.10}$$

The parameter $\xi_{GL} = \frac{\hbar^2}{2m|a|}$ that appears above in Equ. 2.10 emerges from the normalization of the GL equations. It is known as the coherence length and plays a very important role in the characterization of superconductors and we can finally clarify the meaning of the GL parameter κ. The connection between the London penetration depth λ_L, the GL parameter κ and the GL coherence length ξ_{GL} and the critical magnetic fields are given in the following

$$\kappa = \frac{\lambda_L}{\xi_{GL}} \tag{2.11}$$

$$B_{c1} = \frac{\Phi_0 \ln \kappa}{4\pi \lambda_L(T)^2} \tag{2.12}$$

$$B_{c2} = \frac{\Phi_0}{2\pi \xi_{GL}(T)^2} \tag{2.13}$$

Values of $\kappa < 1/\sqrt{2}$ and $\kappa > 1/\sqrt{2}$ thus clearly distinguish between the type I and type II superconductors, respectively.

Type I superconductors

A type I superconductor, by definition, is a material that exhibits perfect flux expulsion in its interior. Physically, the Meissner effect arises because resistance-less currents flow on the surface of the superconductor to exactly cancel B throughout the volume of the specimen. Thus, if the applied field H is increased, the surface shielding current will also increase to keep $B = 0$ inside the specimen. There is, however, an upper limit to the magnitude of surface (within a distance of λ_L) shielding currents that a type I superconductor may sustain. The limiting magnetic field is known as the critical magnetic field H_c and the corresponding current density is known as the critical current density J_c [18].

Type II superconductors

Type II superconductors are those superconductors which lose their superconductivity gradually when placed in external magnetic fields. For a type II superconductor, there is a lower critical H_{c1} and a upper critical field H_{c2} If $(H \leq H_{c1})$ the superconductor is a perfect diamagnet exhibiting the Meissner effect, except for the magnetic penetration depth at the

surface, and quantized vortices are excluded from the bulk. If $(H_{c1} \leq H \leq H_{c2})$, the magnetic field penetrates the superconductor via vortices. If $(H \geq H_{c2})$ the superconductor goes into the normal state.

Part II

Experimental Realization

Chapter 3

Experimental setup

The experiment runs on a massive setup of divers devices. The setup can be explained as three distinguished parts, the lower chamber in which MOT can be produced, the upper chamber where cryogenic environment is provided for the superconducting parts and a magnetic transport belt which connects these two chambers [15]. Each of these three will be discussed briefly in the following. Overview foto, from fritz

3.1   The lower chamber and lasers

The experiment begins in the lower chamber which is an octagon steel ultra-high vacuum (UHV) chamber. Six windows at perpendicular axis provide optical access for the laser beams. A turbo pump and a pressure gauge connected to the chamber bring the pressure to about 5×10^{-11} mbar and an ion pump keeps the pressure by constantly evacuating the chamber. Rubidium atoms are provided by six dispensers. The lower chamber is equipped with a pair of MOT coils and several bias coils [26, 27]. Three lasers are involved in creating the MOT for ^{87}Rb atoms and imaging, their frequencies is illustrated in the right part of the fig. 3.1. An isolated wooden box surrounds them to provide frequency stabilization after they are properly locked. The first one is used as a reference laser. A self built external cavity diode laser is frequency modulated and locked to the transition $F = 2$ to $CO\ F' = 1, 3$ which is the cross-over peak of the first and third levels of the D_2 transition of the ^{87}Rb atoms. This transition is used as an exact reference frequency. The main laser referred as the cooler laser is a tapered amplified (TA) diode laser [28]. It is frequency-locked to the reference laser which causes a beat signal. These combined locked lasers, built in the group, provide cold atom experiments with a fine tunable source while the power remains high. The TA laser is also used for optical pumping and imaging [29]. The TA laser is used for the main cooling transition, for optical pumping and imaging. From this laser six cooler
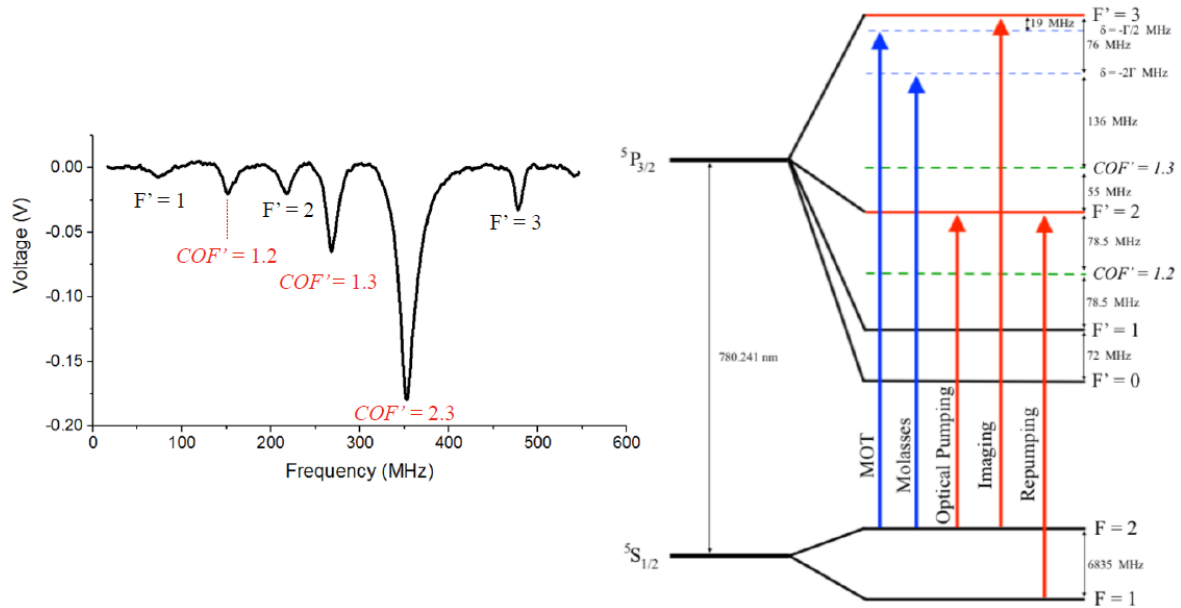
Fig. 3.1 The left part shows a spectroscopy of the hyperfine states in the $^5P_{3/2}$ of ^{87}Rb. The right part shows the laser beam frequencies used in this experiment and the corresponding transitions of ^{87}Rb from the D_2 transition of ^{87}Rb, where F is taken as the ground state and F' the excited state. For example the Mot beam is red detuned by 19 MHz from the transition $F = 2$ to $F' = 3$.

beams with the proper polarization are prepared for the MOT. A picture of the optical table arrangement and the details of the beam preparation is presented in [26]. The third laser, called repumper is a distributed feedback where the grating is formed in the gain region, which can be frequency-shifted by varying the injection current. The repumper is locked to the transition $F = 2$ to $CO\ F' = 1, 2$. Some more information about the lasers can be found in [28, 29]. The repumper is responsible for bringing back the atoms which decay to the ground state (F=1) and get lost from the cooling cycle.

Imaging in the MOT is by a finger camera. The fluorescence of the MOT which is also visible by naked eye is taken as a screen-shot by this life camera. An UHV gate valve separate the MOT from rest of the experiment providing the possibility to upgrade the experimental stage including the chip without losing the MOT [27].

3.2   Magnetic transport of the atoms

The ultracold atom cloud prepared in the lower chamber needs to be transferred to the vicinity of the atomchip in the upper chamber without losing the confinements needed to maintain the atom cloud, therefore the role of an efficient transport is in this experiment crucial. Different ways of transport between the lower and upper chamber has been tried. First method used was the electron beam [30] and then it has come to the conveyor magnetic belt which resulted in a successful transport of the atoms. More details about the efficiency of the transport can be found in [31]. The transport starts in a tube of 7mm diameter which is connected directly to the MOT chamber. The tube gets narrower in the middle to maintain the pressure gradient which also results in losing a fraction of the transported atoms. A pressure gradient of about two orders of magnitude is made by two differential pumping stage [27]. The transport is based on a procedure which addresses arrays of coils. By sending the current to the proper array of coils, the anti-Helmholtz configuration can be reached. Atom cloud can be subsequently moved from left to right till it reaches the corner and then upwards to the vicinity of the atomchip inside the upper chamber (see the setup in 3.3). The controlled movement of the magnetic minimum through the path makes this possible. The magnetic transport starting by the massive push coils, has two main parts of horizontal and vertical transport [26]. Several normal- and superconducting coils construct the magnetic conveyor belt for the atoms. For the horizontal transport four pairs of coils, H1- H4 stand in anti-Helmholtz configuration in an overlapped form 3.2. The part of vertical transport out of the cryostat results from five normal-conducting coils of V1-V5 which can be controlled independently. In the cryostat the superconducting coils V6-V9 are responsible for the final part of the vertical transport. Dividing the transport in two parts and having a corner in the middle of the transport path has this benefit that the final stage of upper chamber can be kept dark from the beams in the lower chamber. More details of the transport can be found in [15, 26, 27].

3.3   Cryostat and the experimental stage

As this experiment utilizes superconducting components considering the last four transport coils and chip wires, cryogenic environment with temperature around 4 K is required. The cryostat here is a Gifford-McMahon with a closed cycle Helium compressor cryo-cooler.

Several different shields cover the upper chamber (see figure 3.3). The outermost shield is at room temperature. Inside it there is an aluminum cylinder to have a high thermal conductivity between its upper and lower part. The cylinder is covered with layers of plastic
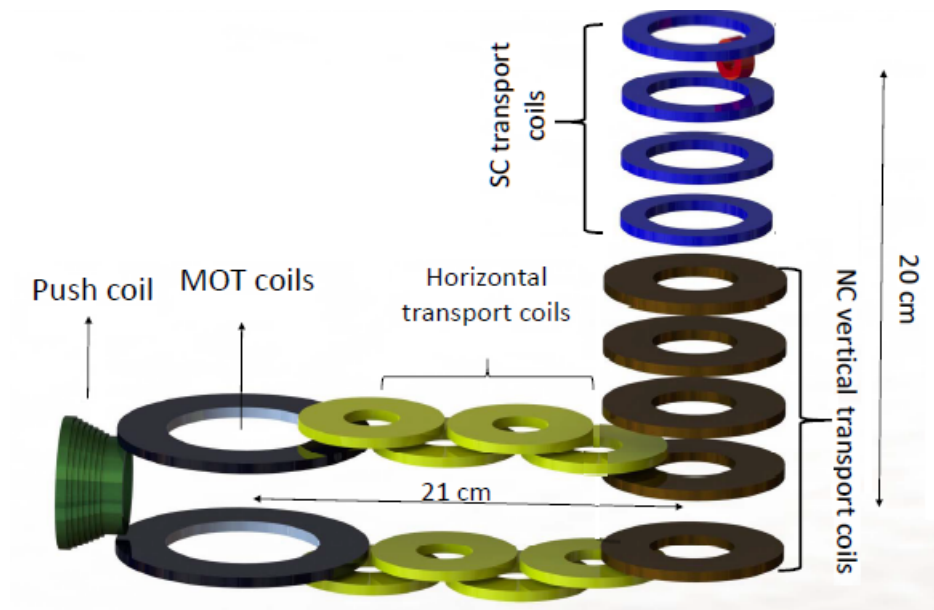
Fig. 3.2 (A CAD rendering of the Magnetic transport taken from [26] which shows the length of each part of the transport path. The massive push coil is needed to initiate the transport. By varying the currents in the coil-pair array, magnetic minimum and hence the atom cloud is moved through the path.

net as a spacer and layers of mylar to protect inner parts from thermal radiations, resulting in a high temperature difference between outside and inside of the shield.The inner part reaches 50 K.

The innermost shield is a PLA [1] -in the institute 3D printed- cylinder and much smaller than the aluminum shield covering the coil cage. The coil cage or experimental stage 3.3 B), contains the last four transport coils V6 - V9, the chip mounting, the Ioffe- and several bias coils. The vertical bias coils are parallel to transport coils. Perpendicular to the mentioned coils are the bias coils in Ioffe direction and bias coils in the main imaging direction. The bias coils are all superconducting. An extra Ioffe coil is added in order to convert the final superconducting quadruple trap into a superconducting quadrupole-Ioffe trap [27].

The superconducting atomchip designed and built for this experiment has a niobium Z-structure. The 500 nm thick Z-wire has a width of 200 μm and a length of 2 mm. In comparison with the normal atomchips which are gold wires on silicon substrates, for this superconducting chip niobium wire is deposited on a sapphire substrate. The chip is mounted on a quartz base which has a zero electrical conductance and high thermal conduction at cryogenic temperatures. The Z-structure has at its to ends niobium pads which are connected to HTc YBCO wires via several Aluminum bonds.

---

[1] polylactic acid

The material for the wire is chosen to be niobium for its high critical temperature among the superconductors. The critical temperature measured for this chip is 9.1 K. In order to supply current to the atomchip, several Aluminum bonds (up to forty) are used from the niobium contact pads towards a commercial HTc YBCO wire [26]
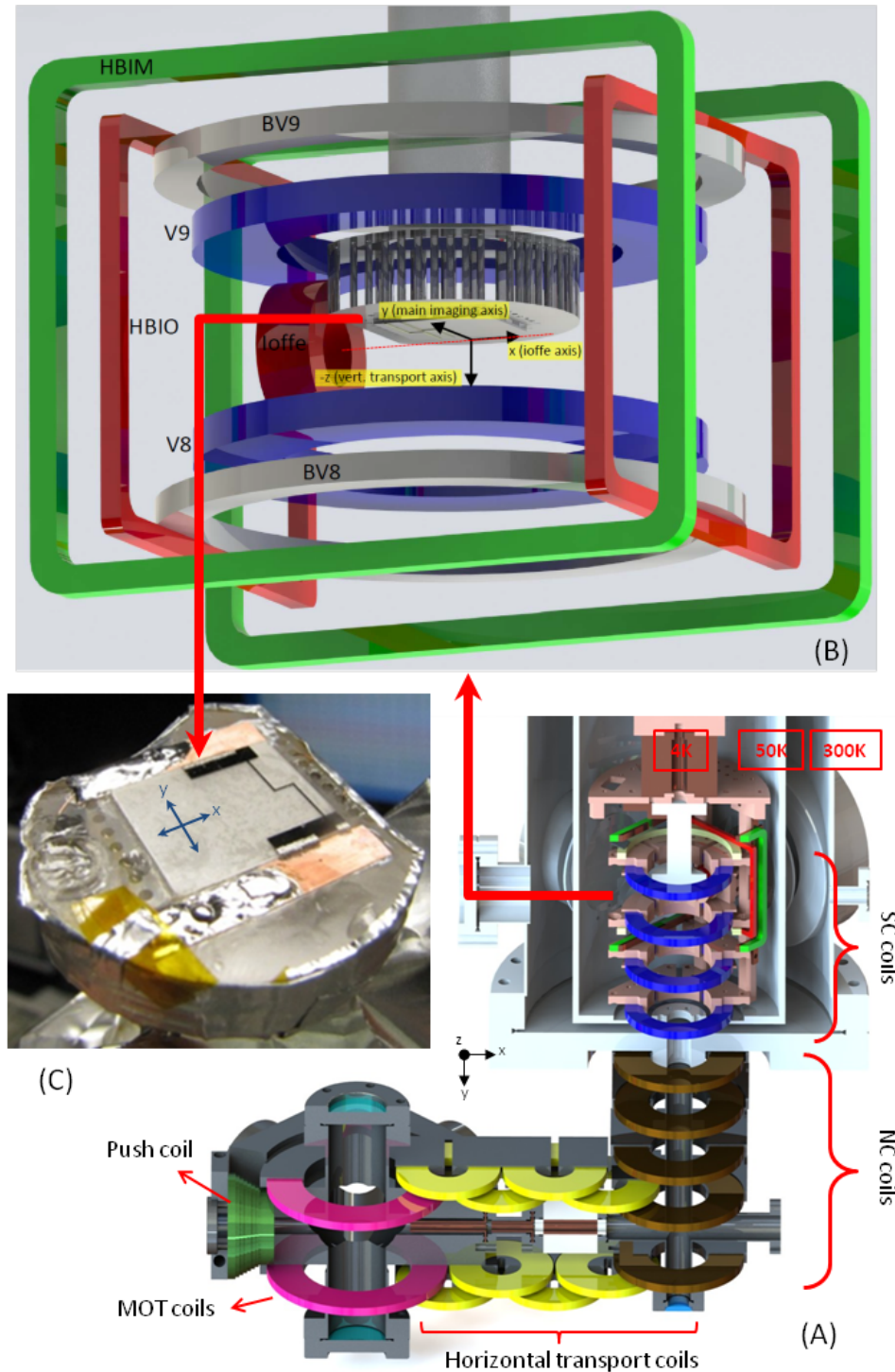
Fig. 3.3 Sketch of the experimental setup. A) overall view taken form [15] including lower chamber from the left in the beginning, magnetic conveyor belt including horizontal transport coils and vertical transport part consisting of normal conducting and superconductor coils. The most upper part of A shows the three shields surrounding the upper chamber. B) CAD rendering of the upper chamber showing all the relevant coils and coil pairs. The quadrupole-Ioffe trap (QUIC) is formed by coils V8 (top blue coil), V9 (bottom blue coil) and Ioffe (red coil). The coil pair BV8 and BV9 (gray coils) can be switched either in Helmholtz or anti-Helmholtz configuration using solid state relays [26]. C) The niobium atomchip on a sapphire substrate with the coordinate axis used here.

3.4 Imaging

The atom cloud needs to be tracked at the different stages of the experiment. Each cycles ends with an imaging. How the imaging is done is through a picture we take from the shadow of the atoms. In the method called **absorption imaging**, a parallel light beam provided by a fiber carrying (almost) the resonant light with the desired atomic transition ($|F = 2\rangle$ to $|F = 3\rangle$) is shined on the atom cloud after a specific TOF (time-of-flight). TOF determines the time interval between the moment the trap is turned off and the first picture which can be adjusted with an accuracy of a ms. The atom cloud absorbs some of this light and reemits it in all directions and the remaining part (showing the shadow of the cloud) reaches the camera on the other side of the imaging system. This is when the first picture of absorption imaging is taken which gives us the I_{atoms}. A high performance CCD camera placed on this side of the imaging system is used for acquisition. The second picture provides a a full image of the beam and is taken when the atoms vanishes from their initial position, giving us the I_{light}. The third picture is taken without shining any light which shows the background noise (I_{dark}). l be divided by the background and finally by subtracting the (yielded) picture missing the atom cloud from the one including the cloud the image will be extracted. As the mean value for the optical density (OD) can be measured from [32]

$$OD_{mean} = ln\left(\frac{I_{light} - I_{dark}}{I_{atoms} - I_{dark}}\right),$$

hence the noise should be subtracted from the first and second picture. Dividing the result then gives us the final picture.

The resolution limit of an imaging system is defined as aperture $1.22 \cdot \lambda$ / 2 *NA* for a circular aperture. The numerical aperture (NA) is a characteristic value of how much light a system can collect. It is defined as $n \cdot sin(\alpha)$, where α shows the angle between the optical axis and the outermost ray that still reaches the camera.

3.4.1 Imaging in the MOT chamber

In our setup we use three different imaging systems. First one allows to make images from the atoms in the MOT chamber. This is very necessary for characterization of the MOT- and molasses performance. Another important use of the lower imaging system is when we optimize the magnetic transport, where we transport the atoms a certain distance and bring them back to the MOT chamber to evaluate losses along the transport.

3.4.2 Imaging in the cryostat

Imaging in the cryostat can be done in two perpendicular directions simultaneously. The transverse direction is called the main imaging axis and the longitudinal direction named as the Ioffe axis.

Main axis

The axis of the main imaging is oriented perpendicular to the axis of the Ioffe coil, as shown in fig. 3.4 left with a white dashed line. It provides a side view of the elongated atom cloud in the QUIC and the chip trap. The imaging system in the main axis is rather simple. It consists of two convex lenses selected in a way that the atom cloud will be in focal length of the objective ($f_1 = 150$ mm), and the camera in the focal length of the second lens ($f_2 = 300$ mm). according to the definition of NA, the less light can be gathered from the emitting source, the worse is the result, so, the highest possible numerical aperture is desired, more explanation can be found in [33].To increase the NA it is essential not to lose rays which managed to come out of the experimental stage in the cryostat. This means to get the first lens as near as possible to the window of the cryostat. The magnification can be calculated from the ratio of both focal length, $M = f_2/f_1 = 2$. The numerical aperture of the main cryo imaging is about 0.26, resulting in a diffraction limited resolution of 1,83μm. With the magnification of 2 and as a pixel of the Pixelfly camera is 6,45 × 6,45 μm, we expect therefore a resolution of about 3.2 μm.

Reflection imaging

The imaging beam can also be tilted such that it reflects off the chip surface as depicted in fig. 3.4 left with a red arrow. With this configuration, we get two images of the cloud, from which the exact distance between the chip surface and the atom cloud can be calculated. As displayed in fig. 3.4 right, the imaging beam hits the chip with the angle (θ) and two images are formed. One of them is formed by the (first) part of the beam which gets first reflected and then goes through the cloud. The second part of the beam going through the cloud before hitting the chip and getting reflected makes the second image. The observed images have twice of the distance of the atom cloud to the chip surface [2].

---

[2]Refer to [34] for the details.

Ioffe axis

The third imaging system is oriented along the axis of the Ioffe coil. The Ioffe direction imaging is very useful to get the position of the atom cloud with respect to the chip wire and to track the cloud through the "swing-by" maneuver, the sequence to transfer the atoms from the QUIC trap to the chip trap. This imaging system integrates along the long axis of the atom cloud, therefore the images are very dense and even very small clouds can be seen. In this setup we use a 50 mm objective lens with 50 mm diameter mounted on the 4 K shield. Using a large lens and mounting it on the 4 K shield to be as close as possible to the atom cloud is to gather the most possible of the parallel rays coming from the cloud. The second lens with the focal length of 50 mm has the half diameter of the objective lens as sketched in fig.3.5. The camera is a DMK 21BU04 USB. As the CCD sensor of this camera is much smaller than the pixelfly we use for the main imaging, we are not able to see the whole range of positions of the cloud as it moves from the QUIC to the chip trap throughout the reloading process. If we want to image the entire sequence without realigning the camera, we use a demagnification system.

Demagnification system

As the imaged object is within the vacuum chamber and the imaging system is on the outside, the minimum distance between atom cloud and the first lens is 87 mm. it became clear that two objective lenses are necessary to circumvent the limited space due to the coils. With one objective lens every setup would lead either to bad aberration behavior or to the need to put the lens there where it is prevented by the coils. A solution was found by setting a lens between window and coils and putting a second lens behind the coils. $NA = D/2f$ D the aperture diameter To calculate the magnifications of the finished imaging setup, a Zemax simulation of the imaging setup has been done. Magnification of $2.7\times$ and demagnification $0.82\times$ has been calculated for the set up sketched in fig. 3.5 and 3.6.
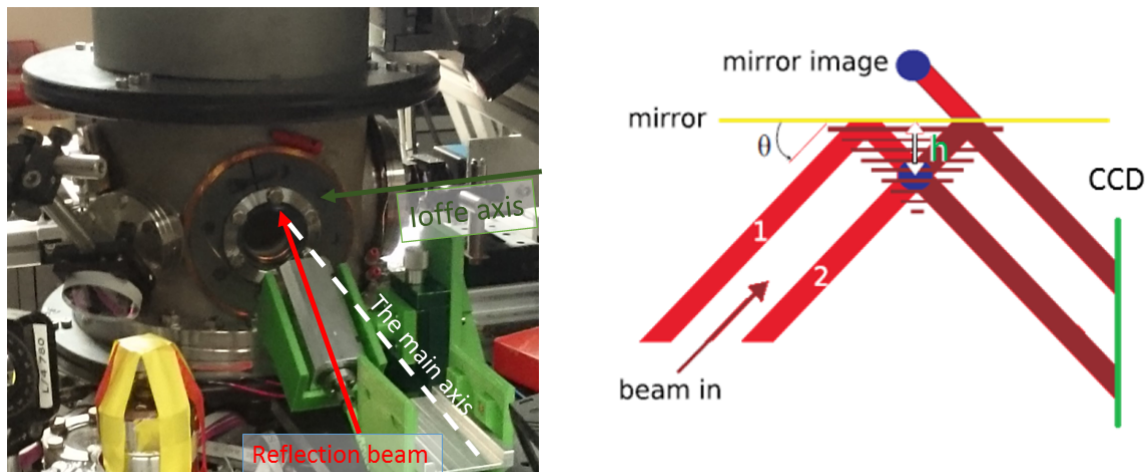
Fig. 3.4 Imaging system in the cryostat. The two imaging axis are denoted with arrows. The right illustration is taken from [34].
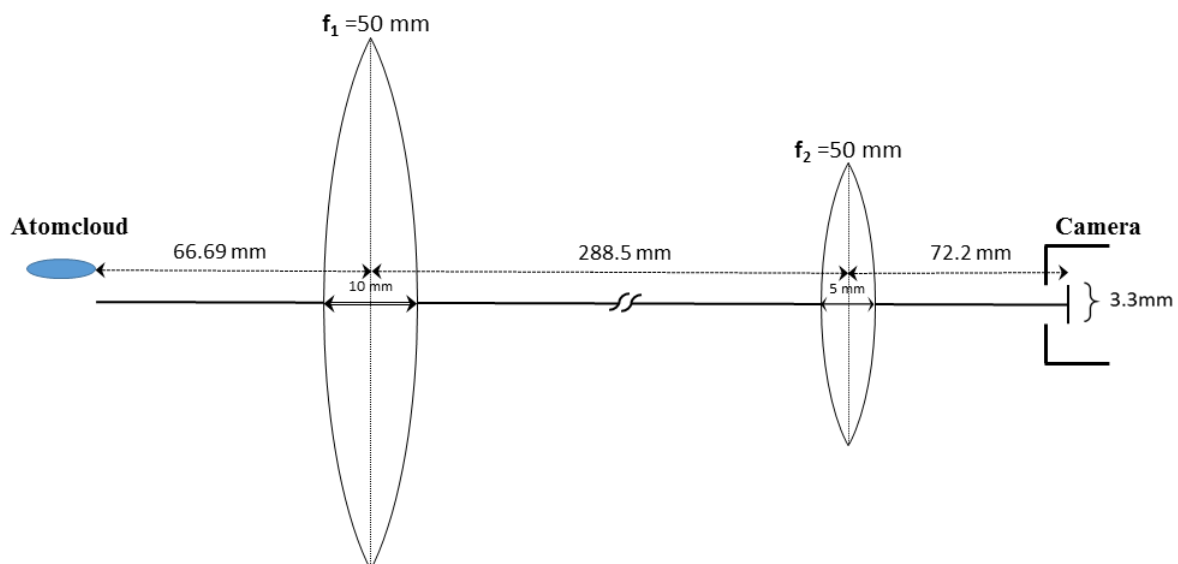

Fig. 3.5 The Imaging system in the Ioffe direction. In this direction the magnification is equal to 2.7.
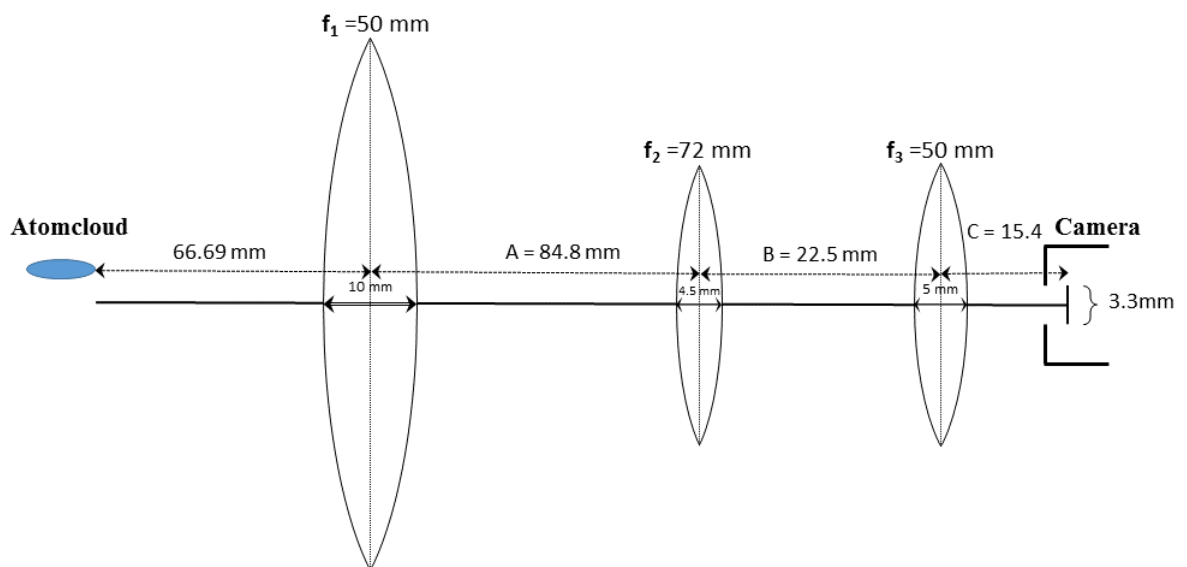
f₁ =50 mm

f₂ =72 mm   **f₃ =50 mm**

Atomcloud

66.69 mm   A = 84.8 mm   B = 22.5 mm   C = 15.4 **Camera**

10 mm   4.5 mm   5 mm   } 3.3mm

Fig. 3.6 The demagnification imaging system new designed with Zemax. The demagnification is equal to 0.82.

Chapter 4

Operation of the experiment

The complex setup of this experiment described in the previous chapter involves many different devices, like:

- 6 dispensers,

- 4 laser diodes,

- locking electronics,

- several AOMs and shutters,

- 3 cameras,

- 6 mot bias coils,

- 6 bias coils in cryo chamber,

- 16 normalconducting coils and

- 11 superconducting coils.

Most of these devices have to be supplied with defined signals in exact time intervals and these parameters need to be programmed. The experiment is done in cycles. Each cycle starts with the initial trapping of atoms and ends usually with imaging of the atom cloud at some position. Many of the devices listed above need to be **controlled** precisely during an experimental cycle. This is done with analog and digital voltage signals[1] provided by an

---

[1] manually controlled on this experiment are only very few components like the main valve (UHV gate valve between the MOT chamber and cryostat), the water valve (for cooling the coils) and locking (unlocking) the lasers.

industrial real-time control system[2]. The system we use has 32 analog- and 64 digital outputs, offering **microsecond precision**. The software of ADwin runs on a program provided by the company. A MATLAB graphical user interface (GUI) allows the user to program the experimental cycles efficiently. The new experimental code wrote by Q. Liang and optimized by T. Weigner to be used instead of ADwin in this experiment is described in details in [31] in subsection (3.8.2).

4.1   Predefined experimental cycles

As mentioned above, the experiment is operated in cycles. The complexity of the setup requires several different types of experimental cycles to optimize the different components. Every cycle starts with cooling and trapping atoms in the MOT chamber and ends with an absorption imaging. Roughly written, depending on what is measured on the experiment, the cycles fulfill one or some of these aims; capturing atoms in the MOT and (or) the molasses (MOT/MOL), transporting them from the MOT till a specif position on the way to the cryostat (Transport forward and return) or into the cryostat up to the vicinity of the atomchip (cryo, cooling in cryo, etc). These need to be specifically programmed and revised depending on the optimization. The cycle can be selected from several GUIs:

- MOT/molasse (M-GUI)

- Transport back and forth (R-GUI)

- into the Cryo (C-GUI).

Each of them are named after the end point of the cycle and will be described briefly in the following[3].

4.1.1   MOT cycle

The M-GUI includes only the MOT, the molasses and the initial magnetic trap, no magnetic transport. All experimental cycles start with a standard MOT. During this phase, the MOT- and MOT bias-coils provide the atoms with the magnetic field, the cooler and repumper beams ensure the required optical field. Directly after MOT, the coils are switched off briefly, and the atoms are further cooled in the molasses caused by the cooler-beam with a shift in its detuning. Followed by an optical pumping, the atoms are brought to $|2,2\rangle$. Without optical

---

[2]ADwin
[3]Quenching the atom chip and the Q-GUI programs for this purpose is discussed comprehensively in [29].
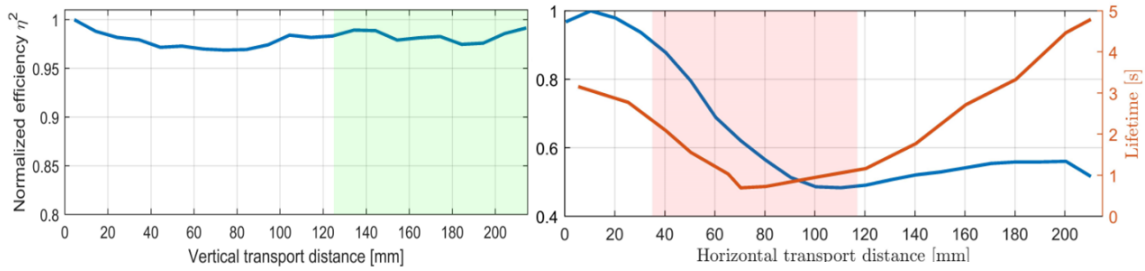
Fig. 4.1 Transport efficiency in the vertical- and the horizontal transport. Left: the green region shows the part inside the cryostat. Right: The red shaded part shows the narrow region of the vacuum tube.

pumping, the atom-number would decrease considerably. Afterwards the cold cloud will be prepared for the transport by bringing atoms in a tighter magnetic field. The cooling and trapping processes rely on many different experimental parameters that can be conveniently optimized using the M-GUI. The optimal settings for the different detunings, etc. can then easily be transferred to the other GUIs.

4.1.2 Transport and return cycle

After cooling and trapping in the MOT chamber, the atoms are moved to their final position by moving the magnetic field minimum they are trapped in. This moving minimum is achieved by a applying the right sequence of currents to the transport coils. This complex sequence, although calculated carefully, still needs some optimization.

In the R-GUI (where R stands for return), we are able to move the atoms up to a defined end-point and bring them back to the MOT chamber where they can be imaged. This process shows how efficient the transport in different parts of the transport path is. For example the fact that the transport-tube gets narrower in around 40 till 120 mm of the transport path causes an obvious drop in the atom-number and transport-efficiency in this region, see fig.4.1.

Typical results of this part are from about 1.2×10^9 atoms in the MOT, around 5.5×10^8 atoms can be observed in the MOT chamber after transporting them till the corner and then back to the chamber.

4.1.3 Buffer trap and QUIC trap

At the end of the magnetic transport section, the atoms are held by the last two transport coils V8 and V9, both supplied independently by two power supplies. A pure quadrupole trap is not desirable for further cooling as the Majorana spin flip losses would become dominant. We therefore want to transform the trap into a QUIC trap. As explained in chapter 2, this is
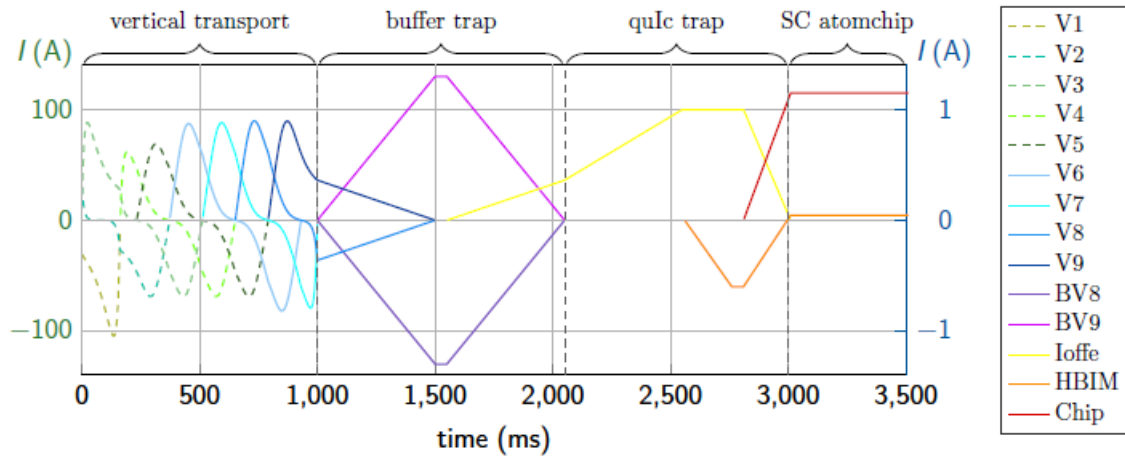
Fig. 4.2 Current sequence for the vertical transport, the buffer trap, the quic trap and the chip trap. Note that the first transport currents here are in normalconducting coils (dashed lines), they therefore refer to the left y axis with much higher currents. The QUIC trap is kept on usually much longer, for precooling before loading into the chip trap. Taken from [5]

achieved using an additional coil oriented perpendicular to the transport axis, the so called Ioffe coil. To avoid vibrations of the trapping potential due to electronic noise in the power supplies, it is good practice to switch the power supplies for the three QUIC coils in series. Current noise on the coils will then cause only mild heating.

In order to switch the coils V8 and V9 in series, the atom cloud needs to be stored in another trap. For this purpose we have a temporary quadrupole trap called buffer trap. The Buffer trap is created by two coils (BV8 and BV9) close to V8 and V9 and is turned on while the last two coils of transport are switched to a series circuit with the Ioffe coil.

The third standard experimental sequence is called the C-GUI, where C stands for cryo. In this sequence, the atoms are transported into the cryostat, then stored in the buffer trap and finally transferred to the QUIC trap.

4.1.4   Loading the atoms into the chip trap

The field lines in the atom chip trap and the QUIC trap are rotated 45 degrees with respect to each other [26]. Our loading sequence accounts for this by using a so called swing by manoeuvre. By applying a negative bias field we move the atoms still in the QUIC trap sideways. With bring the close to the chip with a vertical field B_{vert} and then ramp the horizontal bias field to the desired positive value while ramping down the currents generating the QUIC trap. The entire chip transfer sequence is also part of the C-GUI.
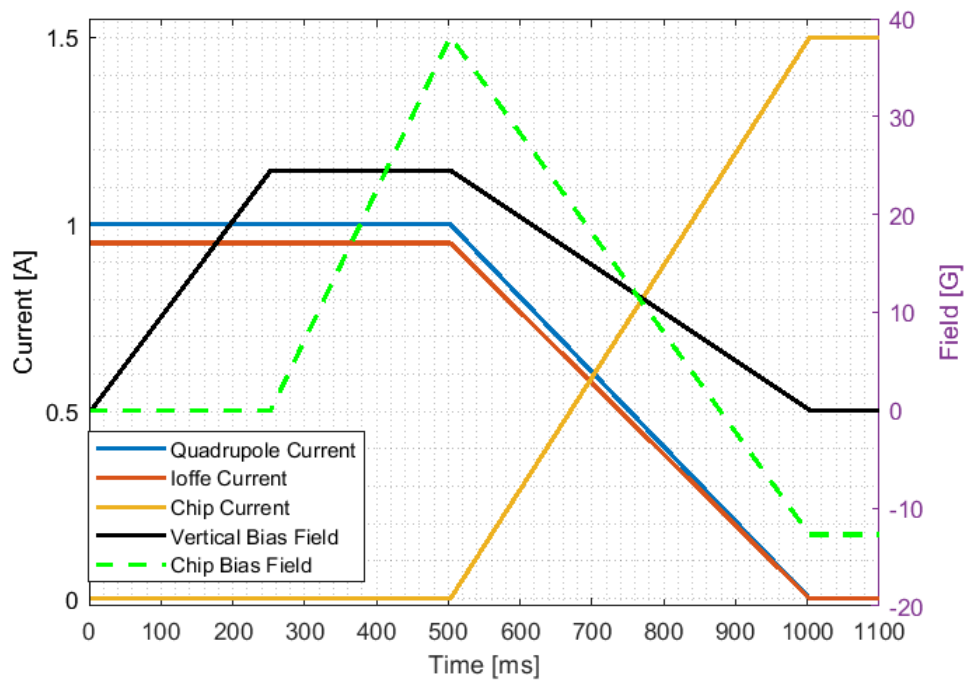
Fig. 4.3 The currents- and fields sequence to transfer from QUIC trap to the chip trap. The swing-by manoeuvre explained in the text can be identified by the chip bias field (green dashed line), which is changing polarity while the QUIC trap currents (blue and red) are ramping down. The vertical bias field is only needed to make sure enough atoms "fall" into the trap.

Part III

Measurements and results

Chapter 5

Towards a Bose-Einstein Condensate on the Superconducting atomchip

In the previous chapter the cycle of the atomchip trap has been discussed. To achieve the BEC in this experiment, an optimized chip trap is required. This chapter contains the required steps to achieve a BEC on the superconducting atomchip.

5.1 Measurements and optimization of atomchip trap

Magnetic traps for the neutral atoms have properties in common on which I will concentrate here. The optimization of the chip trap[1] is done by changing these properties including trap bottom, trapping frequencies and the life time of the trap. Since these optimization are not enough to see a BEC, several stage of evaporative cooling need to be done to increase the phase space density.

5.1.1 Trap bottom

One of the trap characteristics is the magnetic field in the center of the trap where trap has its minimum potential. In other words, the minimum of the field magnitude is called trap bottom. A magnetic trap with vanishing trap bottom can lose atoms due to spin flip. Atoms in this trap are subjected to Majorana spin-flip losses where their spins are so sensitive to field changes (e.g. due to the movements of the atoms) that they can not follow the field's direction adiabatically and get lost of the trap [35]. A quadrupole trap has a zero trap bottom and usually not popular for ultra-cold atom trapping due to these losses at the centre [36].

---

[1]The measurements discussed in this work relates merely to the atomchip trap. For the properties measured and optimized for the QUIC trap in this experiment refer to [29] and [27].

A magnetic field even as small as some milli-Gauss, causes a large enough Larmor frequency for the atoms and will prevent them from spin-flip to untrapped states.

To measure the frequency of the trap bottom, the frequency of the RF signal is changed in a large domain with small steps while the number of the trapped atoms is checked. Starting from larger frequencies, the atom-number decreases slowly till the bottom of the trap is reached with a minimum of the atom-number, where the trap loses the majority of the atoms. It is denoted in fig. 5.1 with a green line. Following the trap bottom spectroscopy from lower frequencies, the sudden drop in the atom-number shows the trap bottom. This is due to the trapped atoms being blind to the radio frequencies below the trap bottom frequency so that these RFs can not affect the atom number in the trap.
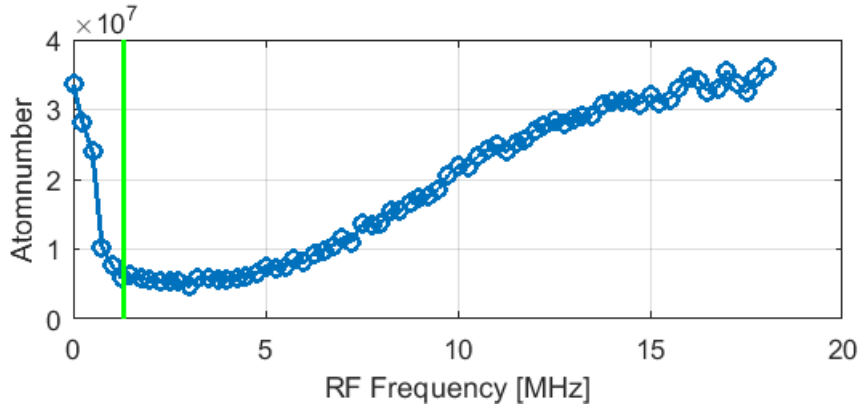

Fig. 5.1 Trap-bottom spectroscopy for the chip trap. Atom-number is scanned for different induced radio frequencies. The sudden drop in the Atom-number marked with the green line shows the Trap-bottom.

The dependence of the trap bottom on the Ioffe field is presented in details in fig. 5.2. The figure shows for higher magnitudes of the Ioffe field, trap bottom has higher frequencies. The right part of the fig. 5.2 shows two samples of several trap bottom spectroscopies with different Ioffe fields. All of these spectroscopies are gathered in fig. 5.2.

The trap bottom spectroscopies for varying Ioffe fields also help us to apply an appropriate Ioffe field which brings the trap bottom frequency higher than the background noise frequencies and leads to more stable chip-trap.

5.1.2 Trapping frequencies

The oscillations of the center of mass in a thermal cloud in a magnetic trap happen at frequencies called trapping frequency [37]. Applying a field pulse on the trapped atoms excites oscillations in the trap and make them oscillate in the harmonic potential like balls
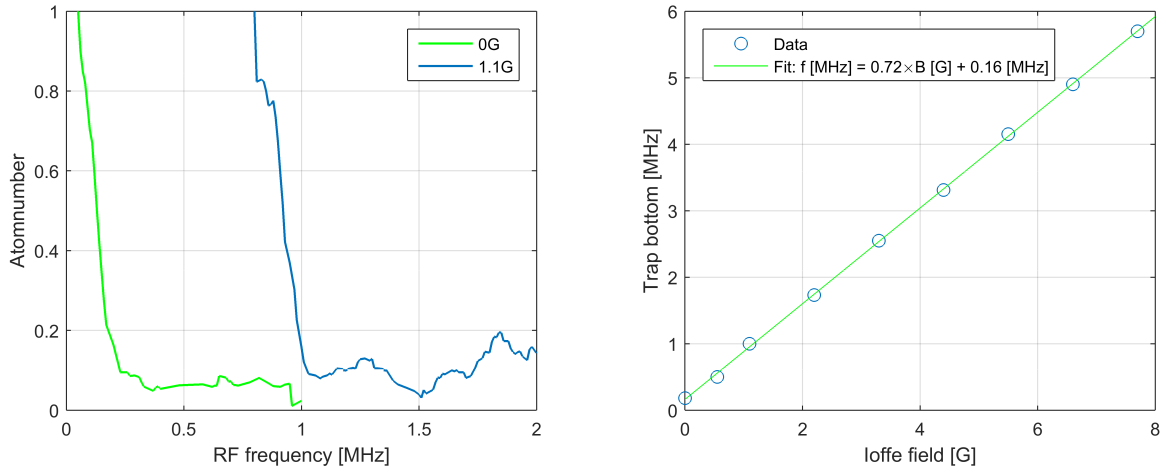
Fig. 5.2 Left: trap bottom spectroscopies for two magnitudes of the Ioffe field, 0 and 1.1 G. Right: trap bottom frequency versus Ioffe field corresponds the written linear fit. Other trap bottom frequencies can be calculated from the Ioffe filed according to this fit.

rolling in a basin. In other words, a field pulse (or equivalently a current spike on the chip current) acts like a "kick" on the atoms, changing their distance to the chip-wire. Since the atoms are trapped in the magnetic trap, they start to oscillate around the minimum of the potential.

For measuring these frequencies, the time after the spike (displayed in right part of the fig. 5.7) is changed and the oscillations of the trap position are measured. One of these measurements constitutes the left part of the fig. 5.7. For a bias field of 10 G, we measured the trapping transversal frequency of 166 Hz which will increase to 400 Hz for a bias field of 20 G.

For the longitudinal trapping frequencies, we need to apply a spike on the current feeding the Ioffe coil. The longitudinal trapping frequency has been measured around 16 Hz for the Ioffe field of 25.44 G.

5.1.3   Lifetime of the trap

Lifetime can be determined by the τ in:

$$N = N_0 \, e^{-t/\tau} \, ,$$

where N_0 is the initial atom-number in the chip-trap. To measure the lifetime of the trap, the atoms are held for a time t_{hold} in the chip trap before moving away for the absorption imaging. Then the atom-number will be measured after the a long TOF, where it reaches
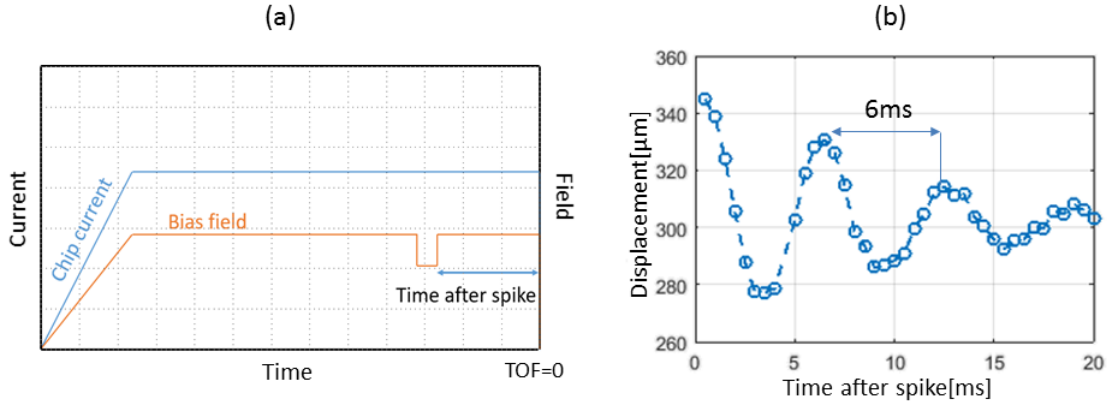
Fig. 5.3 (a): Trapping frequency measurements, a schematic of the filed pulse and chip current to excite oscillation in the trap. (b): The vertical displacement of the chip-tarp over time after the field spike. A Fourier transform of (b) gives the trapping frequency of roughly 166 Hz. The chip current of and bias field will comes here::::

around $1/3$ of its initial value. This long TOF, taken as t_f will be used for the measurements. In these measurements TOF starts from t_f and decreases in steps till 0 where in each step atom-number is recorded by absorption imaging. For the result a double exponential fit will be used.

The double exponential fit has been proven to be a suitable method for the superconducting atomchip lifetime where the Johnson noise is absent [38]. In this method atom number is fit to function of holding time as

$$N(t_{hold}) = A_1 \exp\{(-t_{hold}/\tau_1)\} + A_2 \exp\{-t_{hold}/\tau_2\},$$

where the longer of two decay times, τ_2 is considered to be trap lifetime and τ_1 corresponds to the fast decay due to rethermalization because of surface evaporation.

Fig. 5.4 shows the lifetime measurements performed for the chiptrap. As measurements show, the Lifetime of the chiptrap is rather long, from 60 to more than 90 s depending on the applied Bias fields and the distance of the trap to the chip-surface.

5.2 Multiple RF ramps sequences and phase space density enhancement

The last step to reach the BEC is the forced evaporation cooling where the final goal is to increase the PSD. We employed the same method as describes in details in [39]. Evaporative cooling has to be done with a "RF knife" which can be produced by the current sent to
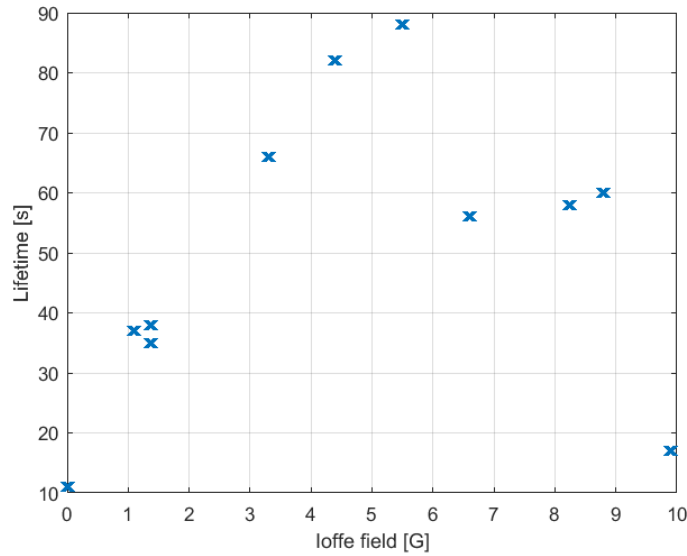
Fig. 5.4 Lifetime for different Ioffe fields in the chiptrap differs between 10 to 90 Seconds. Longer lifetime can also relates to the state where the chiptrap is less sensitive to the noise.

superconducting coils located close to the chip to be able to influence the atoms in the trap. The initial frequency of the knife corresponds to the energy of the hottest atoms in the trap. The RF magnetic field induces Zeeman transition for the hot atoms which are in resonance with the field. The frequency of the knife ramps down so that it corresponds to the temperature decrease.

The RF ramp is made of several linear parts. For each part, three parameters need to be chosen optimally, initial and final frequencies and the duration of the each part. In the first linear part, the initial and final frequency of the ramp can be found out from a spectroscopy like the one performed for the trap bottom, fig. 5.1. Following the atom-number in this figure from higher frequencies, we should set the initial frequency of the first RF-ramp, equal to the frequency where the atom-number (just) starts to decrease, i.e. 16 MHz in fig. 5.1 and 25 MHz in fig. 5.5. The final frequency of this ramp, as discussed in [39], can be chosen as the half width of the frequency distribution, 9 MHz in fig. 5.1. With these choices for the initial and final frequencies, the ramp would release about half of the hottest atoms from the trap, as the atom-number decreases to the half. In this figure can be seen that the fields with frequencies lower than 1.3 and higher than 16 MHz are not resonant with the trapped atoms and no atomic losses are observed. The next parameter to choose is the duration. To optimize the duration, the remaining atom-number (N) and the temperature of the cloud (T) after thet ramps with different duration are applied, should be measured . Calculating N/T^3

which is proportional to the PSD, we then choose the duration in a way that N/T^3 becomes maximum.

Here are some points to be consider in the cooling procedure:

1. When evaporative cooling is applied on a tight trap where elastic collision rate is high, the cooling will speed up. Moreover in a tighter trap the (Zeeman) transition frequencies to untrapped states increases and so the background noise effective in lower frequencies will be minimized, although the confinement of the cloud would then be less.

2. To avoid collision of the cloud with chip surface, the chip gets compressed adiabatically by changing bias fields, before switching off all the magnetic fields.

3. The cooling time needs to be appropriately controlled according to the trapping frequencies: stronger confinement potential needs required shorter cooling time [40].
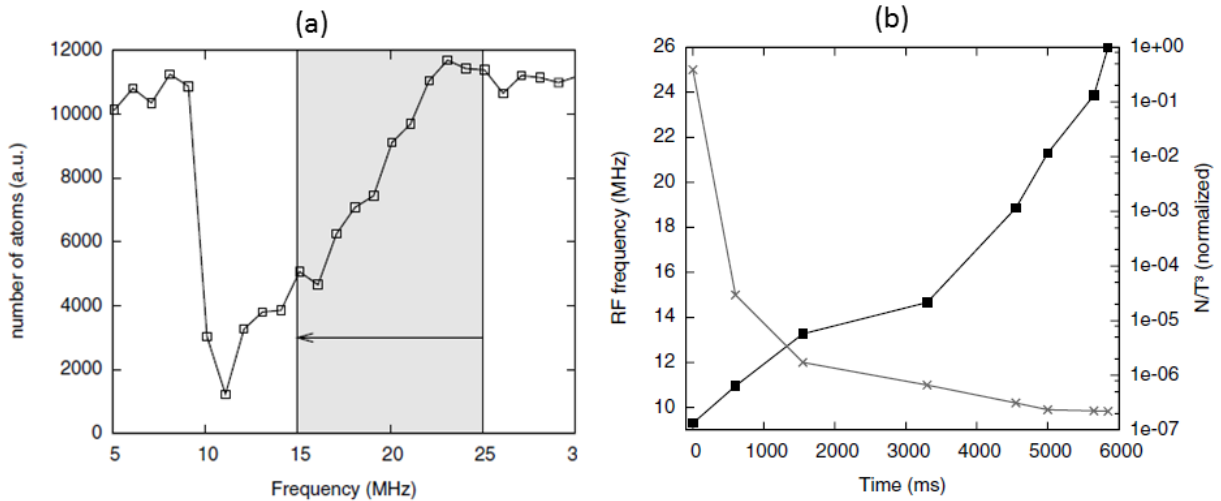

Fig. 5.5 (a): Zeeman spectroscopy of the trapped atoms showing the remaining atom-number over RF field frequencies. The gray part shows the frequencies used for the first ramp. (b): Left part shows the RF knife time evolution. The ramps consist of seven linear parts. Right: The increase of the PSD of in each segment is displayed by the ratio N/T^3 . Overall increase of the PSD is seven orders of magnitude. Both taken from [39].

The evaporation cooling we performed on the chip trap, by two RF-generators applying two linear ramps, caused the phase space density to increase five orders of magnitude. The final temperature reached 280 nK.
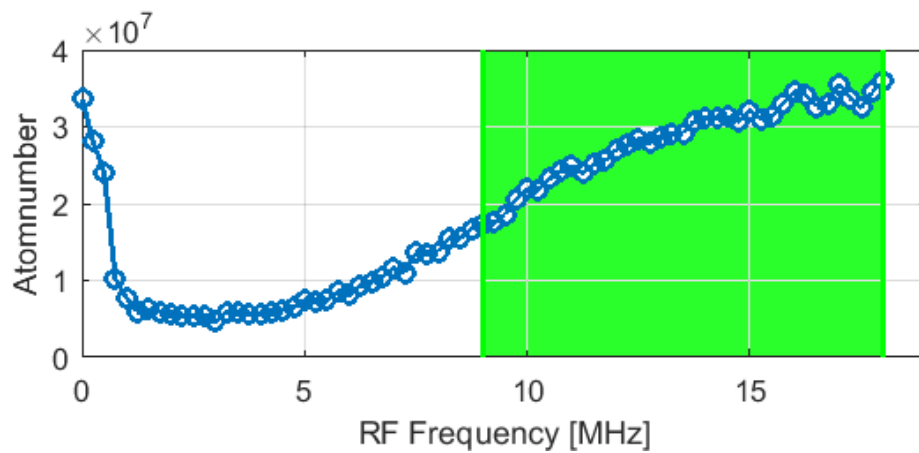
Fig. 5.6 The Zeeman spectroscopy presents an estimation of the energy distribution. It suggests the green area for the first ramp from 16 MHz, where no atom loss is still in the trap to 8 MHz which is the half of the frequency distribution. An RF knife with these start- and end-frequency would cut a significant part of the trapped atoms with the highest frequencies.
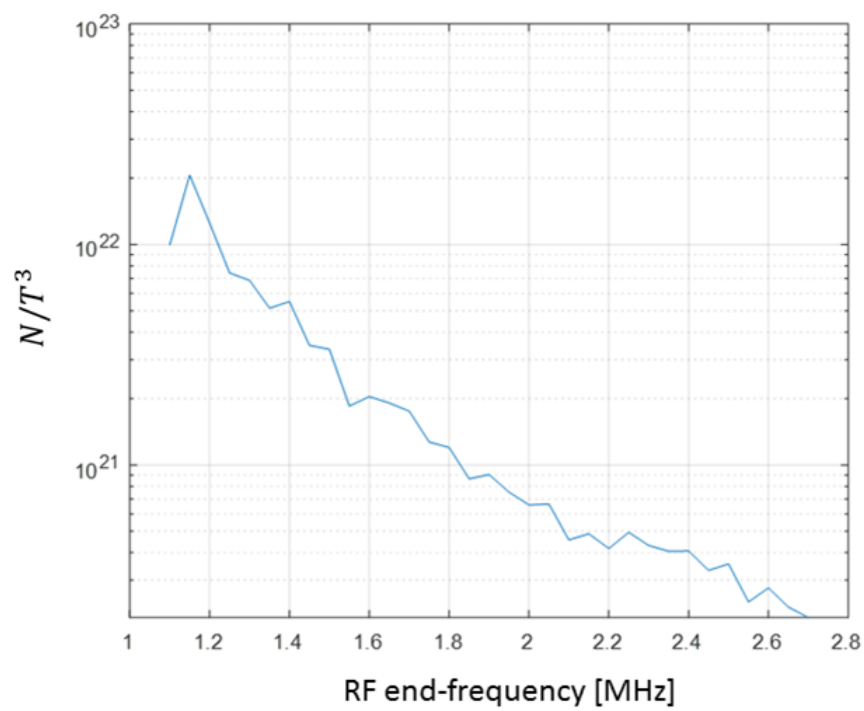
Fig. 5.7 Changes in N/T^3 as a measure of the phase space density over the end-frequencies of RF field. The Increase in the PSD is from 10^{19} to 10^{24} .

Chapter 6

Realizing field-induced remnant magnetization traps for atoms on a niobium structure

Having a superconductor atomchip in this experiment, we are able to examine noble features like utilizing the field-induced remnant magnetization of the atomchip to trap atoms with zero transport current. Some properties of this trap, like its stability and the distance to the chip surface, for different bias field, will be used to understand more about the behaviors of the Nb wire as a type II superconductor in its mixed state.

In the previous chapter, the chip trap is discussed with details. As explained there, in the end of the experimental cycle, a transport current is applied on the chip wire to create the chip trap. In this chapter, we will magnetize the chip externally and then load the chip trap. The absence of the transport current will be compensate by the remnant magnetization induced in the chip, so that the finally created trap, will be remnant magnetization trap induced by an external magnetic field.

In this chapter, we will first provide a short explanation about the formation of field-induced remnant magnetization in type II superconductors, thus, a summary of two types of superconductors. We will concentrate on the type II properties and its description with the aid of critical state model.

The following part is the experimental procedure starting by the magnetization, loading the trap and finally the stability scans collected in details in a table. These long scans show the behaviour of the trap over many hours of measuring scans. Afterwards the scans are investigated in different plots and the influence of magnetization filed applied externally is compared to the net magnet field created on the chip place due to the experimental cycle itself.

6.1   From Meissner effect to creation of remnant magnetization in type II superconductors

A superconductor is characterized with its zero electrical resistance and zero magnetic field. It means a superconducting sample cooled down below the critical temperature, T_c, is completely repellent to magnetic flux. This is due to the supercurrents induced on the surface which cause a magnetic field opposing the applied external field $B = \mu_0(H + M)$ so that $M = -H$ [19].

However superconductors are categorized in two main types depending on their behaviour in an external magnetic field when the temperature is blow the critical temperature. The properties of these two types and the differences between them is summarized below.

6.1.1   Type I superconductors

Abrupt transition at thermodynamic critical field B_{Cth} (or summarized as B_c), where the superconductivity breaks is one of the distinctions of a type I superconductor from type II, see fig. 6.1b. In other words, type I superconductors always expel the field totally for [1]

$$T < T_c \ \ if \ \ H < H_c.$$

The thermodynamic critical field according to Ginzburg-Landau theory is

$$H_c = \frac{\Phi_0}{\sqrt{8}\pi\xi(T)\lambda(T)}.$$

For instance, for a superconducting wire with a diameter d, there is a current which generates the critical field at the surface, given by $I_c = d/\mu_0 \, H_c$

Type I superconductors can be found in metallic elements, with exception of some like niobium, tantalum and vanadium which are type II superconductors.

6.1.2   Type II superconductors

Type II superconductors show a different and more complex behaviour to the external magnetic field B_a. As shown in fig. 6.1a, this behaviour can be summarized in three phases: $B_a < B_{c1}$ Meissner state

---

[1] speaking about applied field, we can take the Magnetic field H and the magnetic flux B here, equal since the magnetization is zero out of the sample, unless it is mentioned explicitly.

$B_{c1} < B_a < B_{c2}$ a mixed state, Shubnikov phase

$B_{c2} < B$ normal state where

$$B_{c1}(T) = \frac{\Phi_0}{4\pi\lambda(T)} \text{ and } B_{c2}(T) = \frac{\Phi_0}{2\pi\xi(T)}.$$

Only for an applied magnetic field of $B_a < B_{c1}$, magnetic flux is expelled entirely form the interior of the bulk.
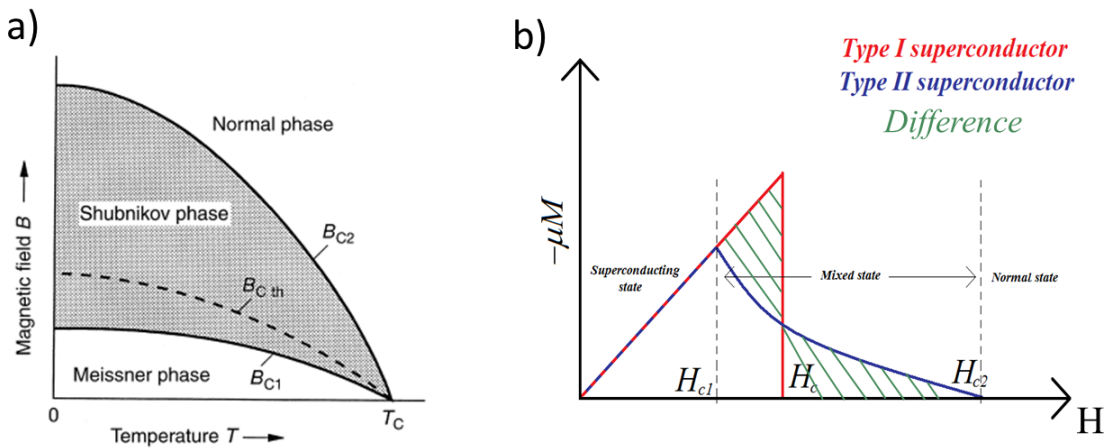

Fig. 6.1 The behaviour of superconductor type I and II in external magnetic field. a) Three characteristic phases for superconductor type II in magnetic field B with respect to B_{c1} and B_{c2}, and for type I with respect to B_{Cth} which is the border of two phases for them. b) Magnetization vs. applied field, correspondence between H_{c1}, H_{c2} and H_{cth}. The difference between type I and type II superconductor is hatched with green [41].

Critical state model of Bean

The critical state model (CSM) describes how shielding and trapping of magnetic flux occurs through flux penetration for the mixed state of a type II superconductor.

What CSM is based on is that there is a critical current density J_c, vortices produce which can flow in a depth on the surface of the superconductor and any force no matter how small will induce this full current to flow. The depth the current flows is just enough to reduce the internal field to zero, $d = \frac{H}{\mu_0 J_c}$. If the applied magnetic field goes above the first critical field (B_{c1}), magnetic flux starts to penetrate in the superconducting bulk.

The flux penetration in the mixed state happens via vortices. Superconducting vortices are normal conducting cores surrounded by circular supercurrents. Each vortex carries a magnetic flux of
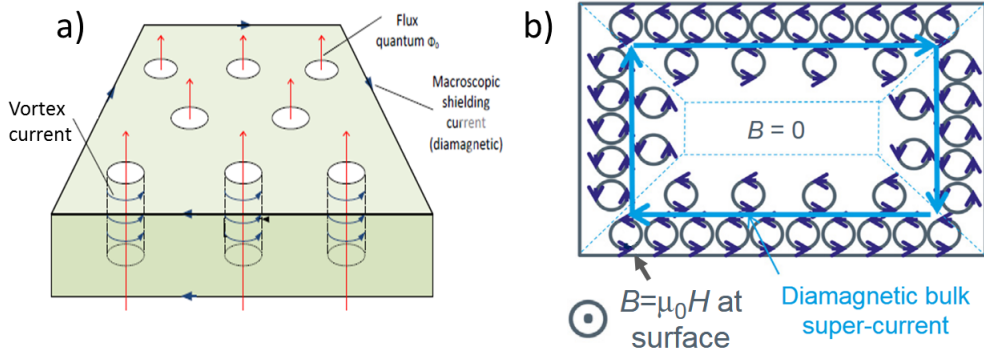
$$\Phi_0 = \frac{h}{2e} = 2.068 \times 10^{-15} Wb$$

Fig. 6.2 Vortices in a type II superconductor from different sides. a) vortex current creates magnetic flux of Φ_0 in each single vortex [42]. b) Penetration of vortices up to a depth of d, leads to a diamagnetic super-current which keeps the field inside the bulk zero.

and the magnetic field caused will be $B = n\phi_0$ which is a "quantization of flux". As the applied field H_a increases, vortices start penetrating from the edges of the superconductor up to a certain depth. In the areas where vortices have penetrated, the distribution of vortices causes a field gradient, the field inside decreases linearly with distance as a consequence of Ampere's law,

$$\nabla \times \mathbf{B} = \mu_0 J \ . \tag{6.1}$$

The external applied field interacts with vortices via the Lorentz force, $F_L = \frac{n}{c}(J_{ext} \times \Phi_0)$, causing them to move in the lattice and an energy dissipation [43–45].
The term J_{ext} refers to the transport current directly or to the current induced by the applied magnetic field H_a, when no current flows through the superconductor.

In the presence of natural defects (or doped impurities) in the superconductor, the vortices may be attached to these defects, which is called pinning effect. The force of the vortex-defect interaction or pinning force can be written in the form

$$F_P = \frac{1}{c}(J_c \times \Phi_0).$$

Based on the mutual repulsion of vortices, the pinning force, F_P depends on vortices density and on the field. The Lorentz force conquers with the pinning force and a resistive state (where there is a dissipation due to the movement of vortices and resistance does not vanish) in a Type-II superconductor occurs if $F_L > F_P(T, B)$.

When the applied field reaches the critical field H_{c2}, the number of vortices reaches a max of $n_{max} = \mu_0 H_{c2} A / \Phi_0$, where A is the area. From this point, the superconductor will be back into the normal conducting state.

When the external field is switched off, vortices are expelled out of the sample so that the magnetic field on the surface becomes zero in the way that the reversed slope in the magnetic field is equivalent to a macroscopic current density of opposite direction. The current density remaining after removing all external fields gives rise to the remnant magnetization of a type II superconductor [6, 46].

6.1.3 Induced supercurrent distribution

Another way of studying the vortex field is through the supercurrent distribution. Due to the memory effect of the superconductor, supercurrents remain in the strip even after the external field is completely removed [6, 47]. The current distribution discussed here is for the external field $B_{c1} < B_a < B_{c2}$, applied normal to the strip-surface and zero transport current flowing through the strip. In this case, the magnetic flux enters from the edges. In the penetrated regions, the current density reaches the critical value of J_c. As the thickness of the Nb-strip is much smaller than its width, $2w$, the current density can be taken constant in the $z-$direction [2]. For simulating the supercurrent density, a sheet current density can be considered in the form of $J(y) = j(y)\,d$ where $j(y)$ is the local current density and d is the thickness.

$$J(y, B_a, J_c) = \begin{cases} \frac{2J_c}{\pi} \arctan\left(\frac{y}{w}\sqrt{\frac{w^2-b^2}{b^2-y^2}}\right), & |y| \leq b \\ J_c\frac{y}{|y|}, & b \leq |y| \leq w \end{cases} \tag{6.2}$$

where $b = w/cosh(B_a/B_c)$ refers to the half width of the central flux-free region and $B_c = \mu_0 J_c/\pi$ indicates the thermodynamic critical field.

When B_a decreases to its final value, B_0 and $-B_a < B_0 < B_a$, the current density becomes:

$$J(y,\ B_0,\ J_c) = J(y,\ B_a,\ J_c) - J(y,\ B_a - B_0,\ 2J_c). \tag{6.3}$$

Fig.6.3 shows the sheet current density distribution for the applied field $B_a = 2.4B_c$. The blue dot-dashed line shows the current density as B_a increases from 0 to $2.4B_c$, computed from Eq. 6.2. When B_a decreases to zero, ativortices penetrate from the edges which can be described by $-J(y, 0, 2J_c)$ and the red dashed line in the mentioned figure. The minus sign is there to oppose the density in the previous part created by increasing the applied field from zero. The final current density comes from adding these two curves and yields from Eq. 6.3 which is the black solid line in Fig.6.3. The anti-symmetric form of the curves in this figure coincide with the fact that the net current in the entire strip is zero.

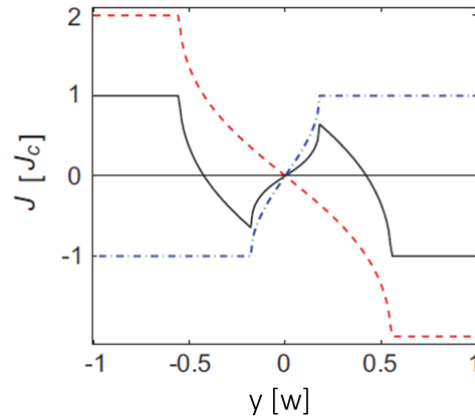[2] see Fig. 6.5a for the axis taken here.

Fig. 6.3 Distribution of the sheet current density is displayed for $B_a = 0 \rightarrow 2.4 B_c$ with the blue dot-dashed line and for $B_a = 2.4 B_c \rightarrow 0$ with the red dashed line. The black curve shows the final distribution. The figure is taken from [6].

6.1.4   Formation of the remnant trap, in connection of the theory and experiment

Simulations illustrated in fig. 6.4 show the formation of the remnant magnetization trap [7]. When the superconductor is brought under the critical temperature and the applied field B_z is smaller than the critical field, the chip is in its Meissner state where it expels every field line, as illustrated in fig. 6.4a. For the applied magnetic field which exceeds the critical field, field lines start to penetrate to the sample via vortices. The vortices remain trapped in the chip after the applied field is off which lead to the remnant field. The distribution of vortices is not isotropic, creating an inhomogeneous field. This field, in combination with a bias field B_x, parallel to the chip surface can trap ultra-cold atoms under the chip and in a radial position as fig. 6.4c shows. In our setup, as can be seen in fig. 6.5a, the superconducting Nb structure can be considered as a rectangular thin film infinite long in the x-direction and $2w$ wide in y-direction. The imprinting magnetic field [3] is applied in the z-direction. The remnant trap is observed at an angle of θ with respect to the perpendicular axis to the chip, more details about it is in section 6.2.3.

In fig.6.5b, formation of multiple traps depending on the induced field-pulse is illustrated. Different directions and time sequences of the applied pulses lead to different geometries of vortices and antivortices and consequently makes the superconductive chip programmable for various remnant traps [8].

---

[3] This field induces magnetization currents in the x-direction that vary throughout the cross-section, y-direction, see the current distribution in 6.1.3.
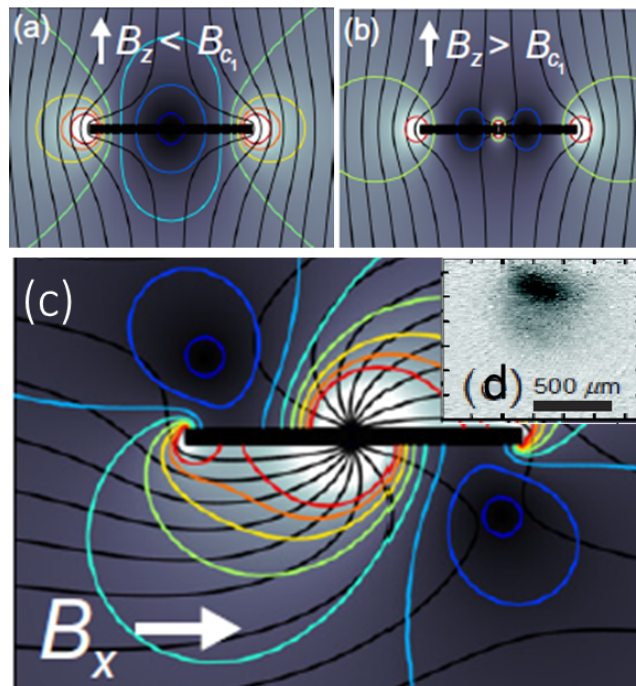
Fig. 6.4 The Potential landscape and field lines simulation showing the construction of the field-induced remnant trap. a) The applied field is smaller than the critical field, field lines are expelled from the chip. b) Magnetic field is penetrated partially in the sample. c) The bias filed B_x in combination with B_z forms the minimum-potential points where the trap can be seen. In all three parts, black lines indicate the field line and colored lines shadow regions indicate the potential, taken from [7].

Before going to the experimental procedure, here are some properties of a niobium sample we should take into account for this work. The first critical field (H_{c1}) is around 140 mT, the second critical field (H_{c2}) 300 mT and the current density (j_c) is 5 MA/cm^2, more details can be found in [48]. The Nb-structure is a Z-wire which is 500 nm thick and 200 μm wide, considered as $2w$ in the y-direction and a Z-length of 2.2 mm which can be taken as infinite long. The critical temperature has been measured as 9.2 K.
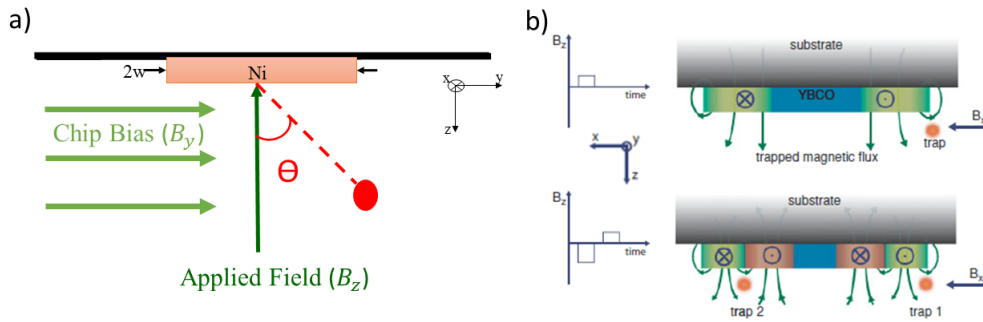
Fig. 6.5 a) The basic schematic resembling our chip-setup showing the Nb-structure and the two substantial magnetic fields responsible for the construction of the field-induced trap, displayed by a red circle. b) upper part: The applied field-pulse in z direction leads to vortices showed by green region. Lower part: a second pulse applied in the opposite direction imprints antivortices showed by pink regions in the YBCO structure. Adding a bias field B_x causes then the formation of two separated traps. b) is from [8].

6.2 Experimental procedure of the remnant trap

The experimental cycle induces a magnetization pattern on the atomchip which should be considered before starting with the magnetization of the chip externally. The magnetic field history includes the fields applied in vertical part of the magnetic transport and the Ioffe and quadrupole field for the QUIC trap. The perpendicular component of net magnetic field on the place of the chip in the center of the Z-wire has been calculated and plotted over time in fig. 6.6. The fields are calculated from the current sequence in the cycle discussed in fig. 4.2. Magnetic fields parallel to the chip surface do not induce a magnetization as the approximation of thin film can be applied for the niobium structure. Thus, only the perpendicular component of the magnetic field is responsible for the magnetic history of the niobium structure.

6.2.1 Magnetization of the atomchip

The chip needs to be prepared with the vortices remnant field, before starting with this part of experiment. The Nb structure should be magnetized properly . This has been done out of the experimental cycle. The last two magnetic coils used for transport-cycle, V8 and V9 are connected in series and 1.5 A is applied to the them. The external field applied on the chip-wire becomes, $1.5\,A \times 898\,G/A = 1374\,G$. The field will be perpendicular to the chip surface, only fields perpendicular to the film induces a remnant magnetization.
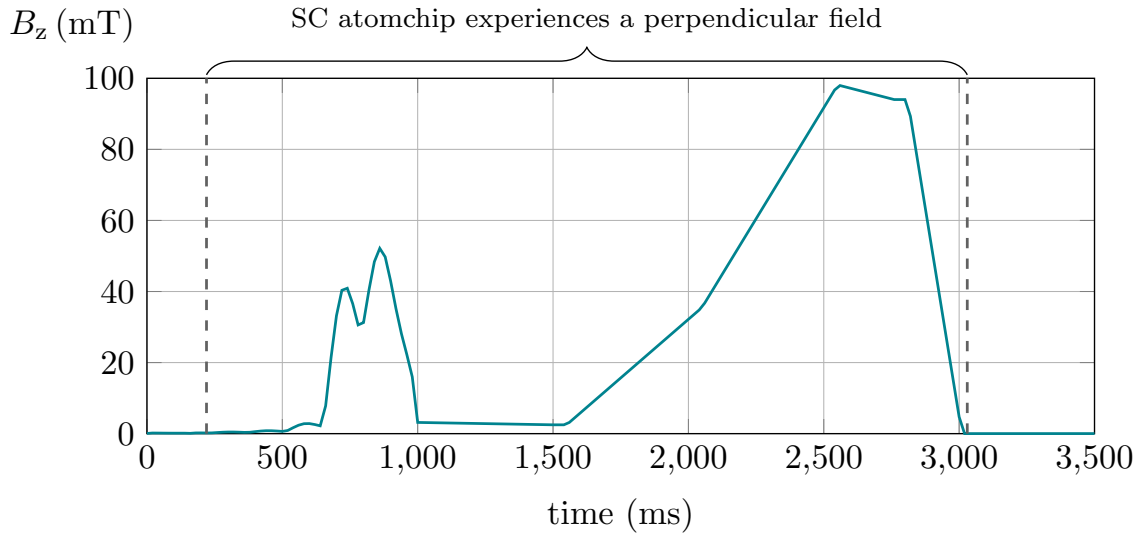
Fig. 6.6 Magnetic field history, perpendicular to the film experienced by the atomchip at the middle of the Z structure. The niobium film experience a magnetic field of almost 50 mT from the magnetic transport. A complete cycle for loading the chip-trap can induce up to 100 mT net magnetic field on the atomchip.

The important point is to be careful about the field strength, so that the final field sensed in the place of chip including the magnetic field from the experimental cycle should be less than H_{c2} or for niobium less than 3000 G or 300 mT. (In higher fields Nb becomes a normal conductor and the imprinted pattern from applied field would be gone.)

6.2.2 Current programming for the pure remnant magnetization trap

After magnetizing the chip, a proper current programming is required to load the remnant trap. As for the field induced remnant trap no transport current is used, calculation and many attempts had to be done to find the trap. The attempts have been done changing the bias fields and perform TOF scans from the end of the QUIC time to follow the trap. The field line simulation e.g. the one in fig. 6.4 has been used to program the loading sequence.

As fig. 6.7 shows, loading into the remnant trap utilizes also the same procedure discussed for the chip trap and represented in fig. 4.3, till the chip current ramps up. The difference is displayed in the magnified part in fig. 6.7. The zoomed area in this figure shows that right before the QUIC-series current is ramped down, two fields of (negative) chip bias and vertical field are applied. The latter plays the role of moving sideways in y- direction and also close to the chip respectively. Afterwards, applying the chip bias field opposite side, positive B_y and meanwhile ramping down the QUIC-series and the Ioffe current would built
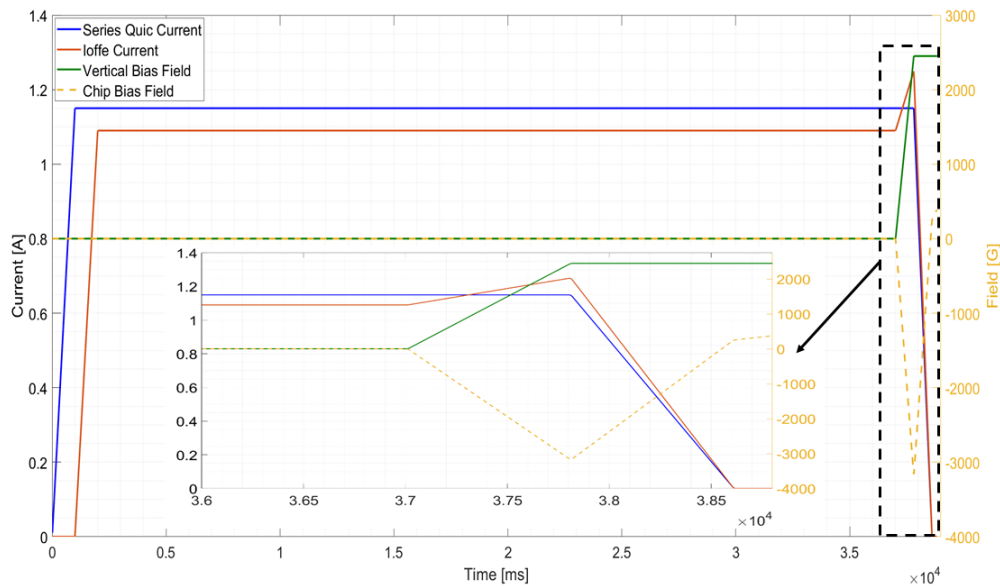
Fig. 6.7 Current sequence for loading into the remnant magnetization remnant trap. The inset shows currents and fields at the end of the cycle, which make the difference between the chip trap and the remnant trap.

the remnant trap. (while applying the first two fields mentioned, the Ioffe current needs to increase first to create a field in the *x*- or Ioffe direction.)

6.2.3   Field- Induced vs current- Induced remnant magnetization trap

Fig. 6.8 presents the field- and current-induced remnant magnetization traps. As indicated in [5], one of the evidence of the remnant trap is the position of the trap relative to the wire center. The different symmetry of the current- and field-induced magnetization is the origin of this evidence. Field-induced magnetization is asymmetric whereas current-induced is symmetric. This means the trap formed by a current-induced magnetization moves symmetrically straight towards the center of the wire-width as the bias field increases.

The other dissimilarity between two types of remnant magnetization trap is how the distance of the atomcloud to the chip surface changes with different applied bias fields. This will be discussed in following section and displayed in fig. 6.11.
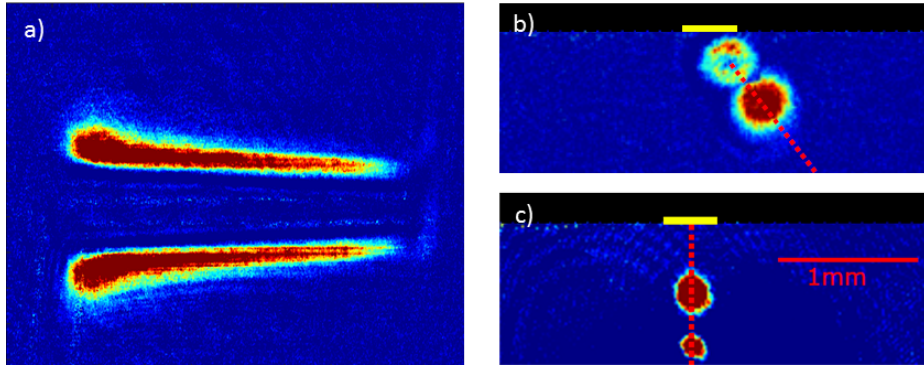
Fig. 6.8 Absorption images of the remnant trap, a) in the transversal direction and reflecting mode, b) and c) in the longitudinal direction. b) shows the field-induced remnant trap and c) is the current- induced remnant trap. The trajectories of the atomcloud toward the chip are displayed for increasing bias field. The yellow line shows the cross section of the niobium wire. Remnant traps in b) and c) are for bias field of 10 G and 30 G.

6.2.4 Stability measurements

After observing the remnant magnetization trap, the question is how stable this trap is during long measurements. To see this, we carried out a group of measurements on the stability of the trap. For this aim, the distance of the trap to the chip has been checked at the end of each experimental cycle. The measurement has been done like all other distance measurements with our setup in the reflection mode. In this mode, the imaging beam hits the chip with an angle so that two images are constructed. In one of them, the beam goes through the trap before hitting the chip, gets reflected and the absorbed image will be gathered after it gets reflected. The other image will be built by the beam which gets first reflected and then goes through the trap. This method gives the distance of the trap to the chip within an accuracy of micrometers, more details can be found in [34].

The measurements are in 4 series, as demonstrated in table 6.9. For each series, the atomchip has been quenched. This was done with the specific laser adjusted for this aim, discussed comprehensively in [29], to hit the superconductor part of the chip (middle of the Z) and quench it by heating it up above the critical temperature locally so that Nb-structure returns to its virgin state, erasing its magnetic memory.

First series starts after the quench, with a magnetization of 1.5 A of the coil current which is equivalent to a coil field of 1374 G. Here the distance scans start after some TOF scans which have been done for optimization the remnant trap.

The next series starts with a very weak magnetization field of about 450 G and the distance is measured for bias fields of 3, 5, 9 and 11 G, the second row in the table 6.9. Third row contains the longest measurements. The magnetization is like in the first series, 1.5 A so that

Measurement's series	Magnetization		Operational Details	Scan Number	Bias Field	Shots (Nr.)	Scan Number	Bias Field	Shots (Nr.)	Scan Number	Bias Field	Shots (Nr.)	Scan Number	Bias Field	Shots (Nr.)
	Amper	Gauss													
1	1,50	1347	some TOF scans before	11	3	202	12	5	200	14	9		15	11	65
2	0,5	449	Started directly after the quench	21 / 22	3 / 3	50 / 150	24	5	200	26	9	200	25	11	95
3	1,5	1347	Started directly after the quench	27	3	200	28	5	440				29	11	200
4	1,8	1616	Started directly after the quench	31 / 32	3 / 3	80 / 123	33	5	200						

Fig. 6.9 Measurements performed with the Field- induced remnant magnetization trap. Each raw of scans begins with a magnetization which is done after the chip has been quenched. Number of shots indicates the numbers of successfully loaded cycles with an image of the trap at the end which shows how many distance-measurement is included in that scan. As each cycle takes around 60 seconds, a scan with 200 shots takes more than 3 hours. Scans 22, 27 and 31 are fresh measurements after the quench which have more than (at least) 80 shots.

the influence of being freshly quenched (or existing many scans before) can be seen in the distance. This different history leads to an increase of the distance. For the bias field of 3 G, the distance in scan 11 is on average 6 µm more than the distance in scan 27 which has its average around 212 µm, see fig. 6.12a. This is due to fact that the magnetic field sensed on the chip place because of loading cycles (as fig. 6.6 shows), acts like an imprinting field and changes the magnetic history of the chip. The longest scan has been done with 440 shots. "Number of shots" indicates how many cycles have been run successively till end and imaging has been done at the end.

The longest scan performed with the remnant trap can be seen in fig. 6.10. With 440 cycles of 60 second duration, this scan makes it possible to observe the stability of the trap within long time measurements. The influence of running cycles on our measurement perturbs the distance of the trap to the chip up to some microns over several hours. Each one of the cycles can produce a perpendicular magnetic field between 500 to 1000 G and can take 58 seconds plus about 2 seconds needed to start the next cycle. In this scan the trap distance to the chip increases from 165 µm in the first shots to 180 µm in the last shots. It shows that the net magnetic field caused by loading field can have a considerable roll as an imprinting field for a measurement taking more than 7 hours.

The last series has the highest magnetization field of 1.8 A and measurement has done for two bias fields of 3 and 5 G. In figs. 6.12a and 6.12b, these measurements are displayed separately for two different bias fields. In these figures each point indicates the average
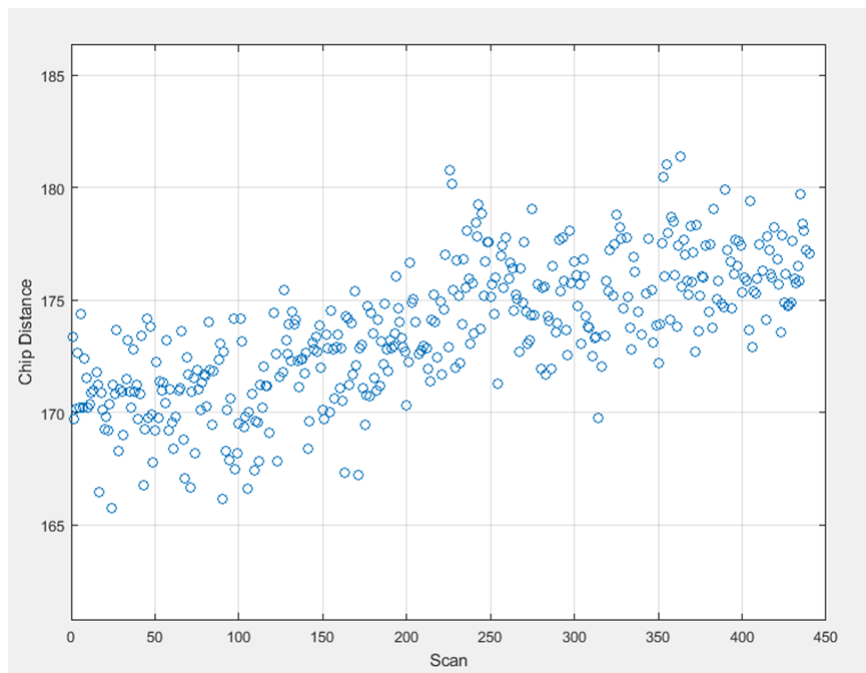
Fig. 6.10 Influence of the loading cycle on the distance of the trap to the chip-surface over a very long measurement. The distance-measurements have been done for more than 440 times running the experimental cycle, each taking around 60 seconds. All loading-parameters are kept constant during the scan. An increase of about 15 μm can be seen in the raw results.
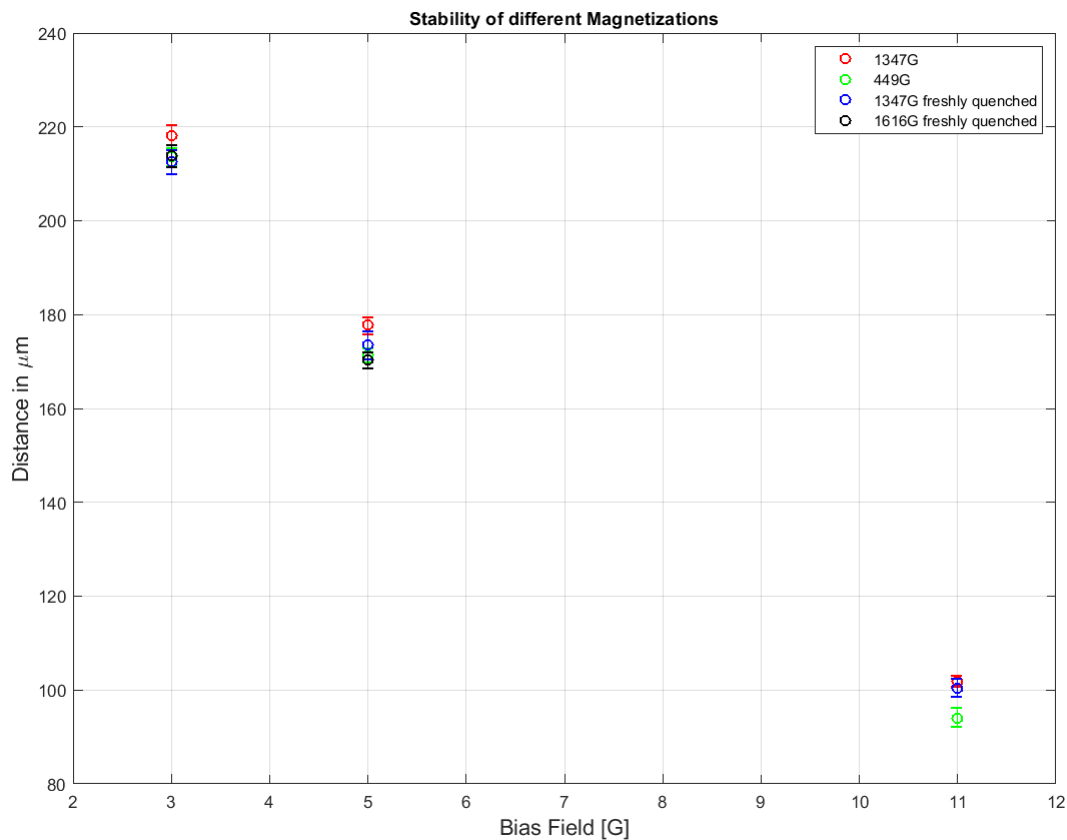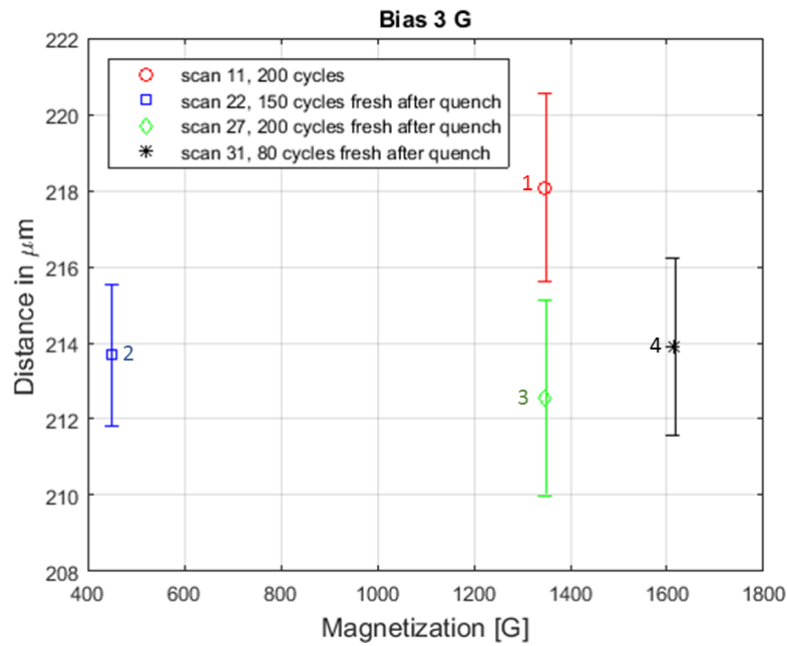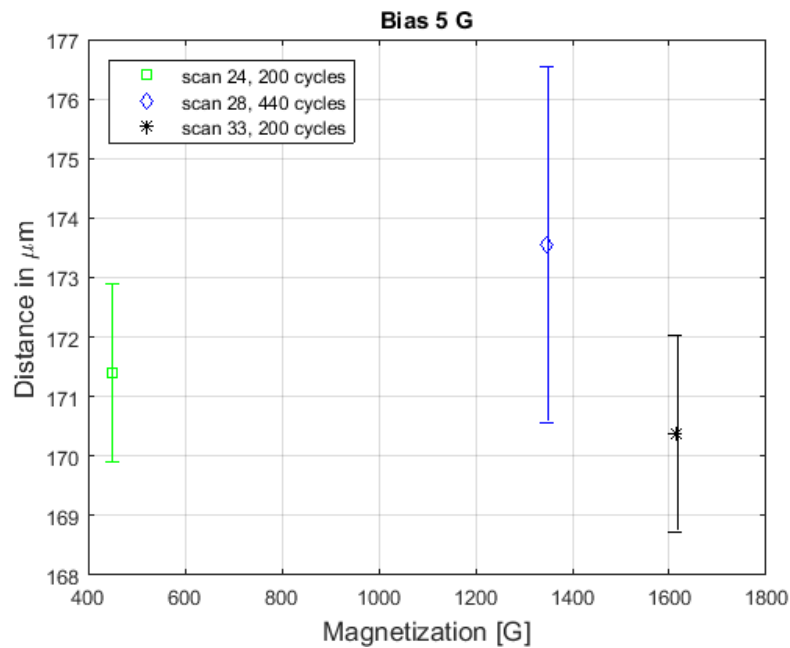
Fig. 6.11 Distance of the remnant trap to the chip surface versus bias field averaged over the many cycles included in one scan. The trap is purely field-induced, the variation of the distance for different magnetization and during these long scans is minor compared to the differences of distances for various bias fields.

distance over all the shots of the scan with the standard deviation from these values. Fig. 6.11 shows the distance measurements over bias field including different magnetization fields. This is to compare with the results of fig. 7.11 of [26]. The point here is the zero transport current. What is responsible for this trap is the bias fields in combination of the magnetic field, the remained vortices induced which leads to stable remnant trap as can be seen from trap-chip distance.

(a)

(b)

Fig. 6.12 Distance of the remnant trap to the chip surface for different Magnetization fields. Each point shows the average distance in all of the cycles taken in that scan and the standard deviation of it. Less than 5 μm variation in a distance of around 200 μm in (a) and around 170 μm in (b) shows a stable remnant trap whose distance does not vary significantly in time (scans-duration), nor with magnetization fields of theses scales. In (a), the numbers (1-4) show the series the scans belong to (shown in the table 6.9). The difference between 1 and 3 here is the different magnetic histories of these two scans.

6.2.5 More discussions on the remnant trap measurements

Fig. 6.12, includes the overall average over the results of all cycles in a specific scan and the standard deviation of it. For some measurements, this kind of averaging does not include the local changes, e.g. when there is a drift in the measured parameters which is obvious in 6.10. In these cases, an appropriate domain needs to be determined for averaging and the deviation is then calculated from this local mean value.

To see the difference of two averaging methods in detail, I start with the definition of the standard variance. The standard variance is defined as

$$s^2 = \frac{1}{N-1} \sum_{i=1}^{N} (y_i - \bar{y})^2$$

where y_i is the i-th of M measured parameters and $\bar{y}$ is the average of this parameter. The standard variance is usually expressed as its square root, the standard deviation, s. It is not recommended as a measure of stability because it is non- convergent for some types of noise commonly found in some sources, like frequency [49, 50] or when a measurement shows a drift after a specif number of sampling. The problem can be solved by instead using the Allan deviation.

Allan deviation

Allan deviation, originally used for making atomic clock better, is the most common time domain measure of frequency stability [49]. If a specific clock drifts, then it's not recommended to average over a large number of data points. The Allan deviation gives the minimum or maximum sample size we can average to get the lowest possible standard deviation such that we don't account for the drifts in a considerably long measurement.

The Allan deviation is intended to estimate stability due to noise processes and not that of systematic errors or imperfections in frequency-domain measures, or time-domain measures [51]. More exactly, the non-overlapped Allan, or the 2-sample deviation, is used as the standard time domain measure of frequency stability [52, 53]. The Allan deviation is the square root of Allan variance which is defined as:

$$\sigma_y^2(\tau) = \frac{1}{2(M-1)} \sum_{i=1}^{M-1} \left[y_{i+1} - y_i \right]^2$$

where y_i is the i-th of M measured values averaged over the sampling interval τ.

Fig. 6.13 shows a 200-shots scan of the remnant trap distance to the chip and its Allan deviation. The way Allan deviation is used here is that, as figs. 6.13 and 6.14 show, the

calculated Allan deviation in the lower part of these figures has a minimum of deviation at a specific point which is taken as the "window". The window is then used in the upper plot as the number of samples (shots) over which the mean value and the standard deviation of the distance are calculated. In figs. 6.13 and 6.14 two completely different behaviour of the Allan deviation can be seen. In fig. 6.13, the Allan deviation will be smaller when measurements number increases and it has its minimum when the window is 83. In other words, averaging over a larger number of samples gives a small deviation which indicates that this scan shows stability during all included cycles in a time interval of over 3 hours (200 shots, each 60 s).
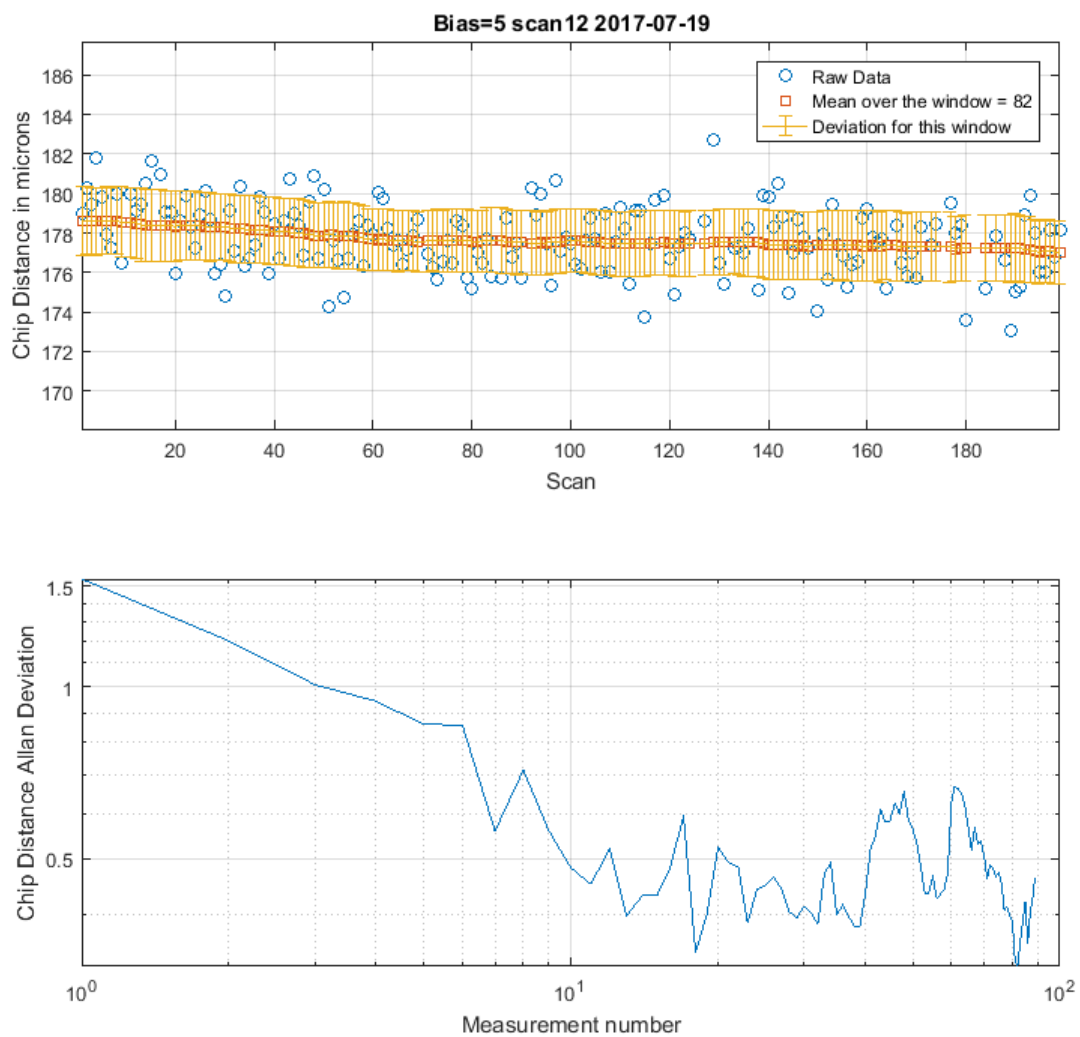
Fig. 6.13 The distance of the trap to the chip and the Allan deviation of the distance for a scan with 200 shots. The Allan deviation of the chip distance has a minimum at 82. This minimum is taken as the window in the upper part. The fact that the number taken as widow is large shows the stability of the remnant trap in times range of more than 3 hours.
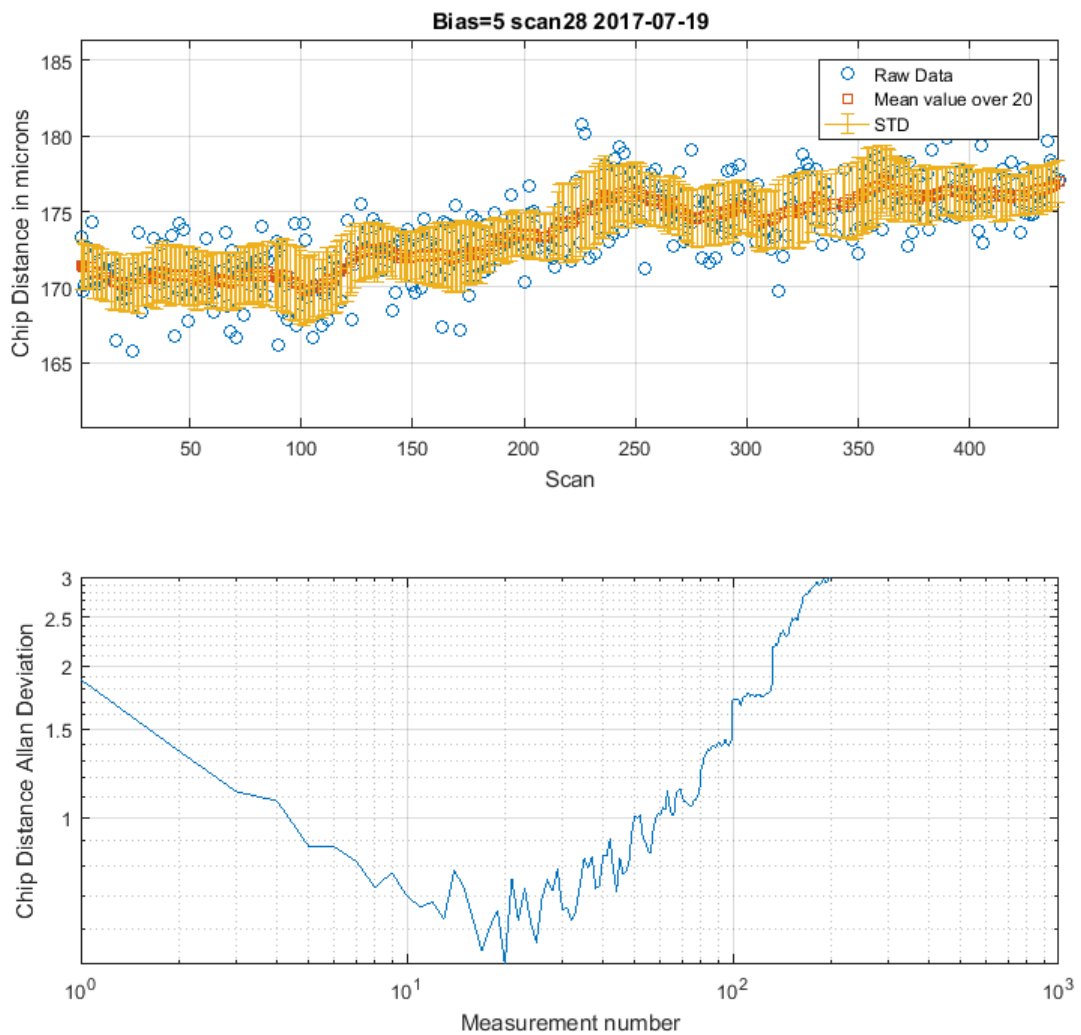
Fig. 6.14 One example of seeing drift in the measurement. This can be deduced from the Allan deviation plot, as the windows here is very small (20) in comparison to the shot number (440).

Dependence of the distance-drifts on the time-order of measurements

In the beginning of this section, the drifts in the distance in long measurement is mentioned where Allan deviation is employed to have a better averaging of the results. Here the drifts are investigated carefully. We want to find out if the order of the measurements after quench affects the result.

looking into all the distance scans collected in table 6.9, we see that regardless of the bias field applied, there is a similar trend in the scanned distance depending on how long the

cycle has been running after the quench. The quench in the beginning of each series acts as a complete reset of the remnant magnetization history. In the measurements carried out freshly after the quench and demonstrated in fig. 6.15, the distance reduces gradually in the Consecutive shots of a scan. The order of this reduce is in order of 3 to 5 percent of the distance, see fig. 6.15.

After this reduction, the average [4] of the distance stays constant. This stable behaviour can be seen in scan 12, fig. 6.13.

If we continue measurements without quenching the chip, the distance will be increased. This tendency happens after around 400 cycles (6.6 hours) from the quench and can be seen in scans 26 and scan 28. Noticeable about scan 28 is that as it contains more than 400 cycles, both trends of being stable and increasing distance can be observed, see fig. 6.14. This shows that these trends do not depend on the bias field. The distance-drift depends on the numbers of running cycles before, in other words, on the remnant magnetization history of the chip.

To explain this behaviour, we recall fig. 6.6 which shows the magnetic field the Z-structure experiences due to one experimental cycle, $B_{cycle} = 50$ up to $100 \ mT$. Assuming the critical field for niobium to be $140mT$, each cycle acts like an external field of around $B_c/4$ on the Z-wire. The distribution of current density when an external field is applied, is discussed in sec. 6.1.3. As can be seen with more details in figure 7.3 of [26], a field magnetized wire can be considered as two wires with a certain space, carrying opposing currents. Hence by running the cycles after the magnetic history is erased (quench), the magnetization accumulates. The Meissner effect reduces the distance and causes the first trend in the scans right after the quench. After that there is a point where the magnetization gets saturated and this is the point where averaged distance stays constant.

---

[4]It should be noted that the average used here is the average with respect to Allan deviation and not the common standard average.
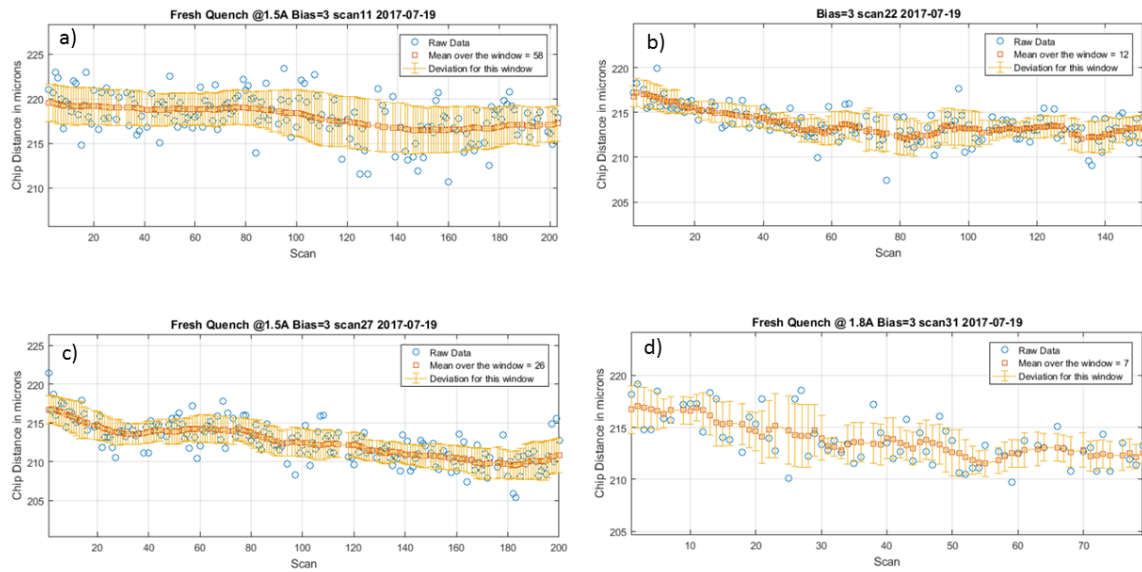
Fig. 6.15 The distance of atoms to the chip reduces in the long measurements right after the quench. a) in the first 80 scans, the distance stays constant, then it starts to decrease from shot 80 till 150 so that the average distance changes from 220 to 216 microns. b) distance reduction happens in the first 80 cycles from 217 to 212 microns then stays constant. c) in 180 shots decreases the distance from 216 to 209.5 microns. d) the average distances falls from 216 to 121 microns. In the following scan (not pictured here), which is the continue of scan 31, the distance starts from 218 and decreases to 214 microns.

Chapter 7

Conclusion and outlook

During the time of performing this work, a great opportunity was to learn how to deal with ultracold atoms and superconducting techniques. Many attempts has been done to get a BEC on this superconducting atom chip. These attempts had the result of an optimized trap and increasing the phase space density up to five orders of magnitude with final temperature of $280\,$nK. With seven orders of magnitude increase in the phase space density the BEC has been observed in [39].

One of the promising prospects of this experiment is to use the properties of supercon-ductors to create novel magnetic traps. Regarding this prospect, a remnant magnetization trap purely field induced has been observed with the Nb Z-structure of the atomchip. Many similarities to a YBCO remnant magnetization trap [6, 7] has been observed like the effects of the vortex distribution on the formation of this trap and the stability of the trap. The measurements performed with this trap include several long scans where the magnetization field has been changed several times to see the influence of the imprinting field on the trap, and its stability over time. The distance measurements for this trap refer to a stable trap over time scales of hours which does not response to the higher magnetizing fields. What is to deduce from the long scans is that if an imprinting field like the magnetic field obtained from the experimental cycle which is applied in numerous times can lead to more penetrated vortices and result in more intense remnant magnetization in comparison to the case of applying higher imprinting field at once. In the long run, with a number of repetition of lengthy distance measurements we came to conclusions that after a specific time of scanning, the magnetization get saturated so that the remnant trap stays for a time order longer than needed for our measurements (at least 100 cycles) so stable that the distance to the chip can be estimated with accuracy of 1 micrometer.

On the way to the ultimate goal of having a hybrid quantum system on this setup, the possibility to integrate an atom trapping method that doesn't require an external connection to the outside world shines promising.

References

[1] M. Weidemueller and C. Zimmermann. *Cold Atoms and Molecules*. WILEY-VCH GmbH Co. KGaA, Weinheim, 2009.

[2] R. Folman, P. Krüger, J. Schmiedmayer, J. Denschlag, and C. Henkel. Microscopic atom optics: From wires to an atom chip. *Advances In Atomic, Molecular, and Optical Physics*, 48:263–356, Feb 2002.

[3] C. Henkel, P. Krüger, R. Folman, and J. Schmiedmayer. Fundamental limits for coherent manipulation on atom chips. *Applied Physics B*, 76 (2), 2003.

[4] J. Verdú, H. Zoubi, Ch. Koller, J. Majer, H. Ritsch, and J. Schmiedmayer. Strong magnetic coupling of an ultracold gas to a superconducting waveguide cavity. *Phys. Rev. Lett.*, 103:043603, Jul 2009.

[5] F. Diorico, S. Minniberger, Th. Weigner, B. Gerstenecker, N. Shokrani, Z. Kurpias, and Jörg Schmiedmayer. Current-induced magnetization hysteresis defines atom trapping in a superconducting atomchip. *SciPost Phys*, 4,036, 2018.

[6] B. Zhang, R Fermani, T. Müller, M.J. Lim, and R. Dumke. Design of magnetic traps for neutral atoms with vortices in type-ii superconducting microstructures. *Phys. Rev. A*, 81:063408, 2010.

[7] T. Müller, B. Zhang, R Fermani, K. S. Chan, Z.W. Wang, C.B. Zhang, M.J. Lim, and R. Dumke. Trapping of ultra-cold atoms with the magnetic field of vortices in a thin-film superconducting micro-structure. *New Journal of Physics*, 12:043016, 2010.

[8] T. Müller, B. Zhang, R Fermani, K. S. Chan, M.J. Lim, and R. Dumke. Programmable trap geometries with superconducting atom chips. *Phys. Rev. A*, 81:053624, 2010.

[9] J. Meija, T.B. Coplen, M. Berglund, W.A. Brand, P. De Bièvre, M. Gröning, N.E. Holden, J. Irrgeher, R.D. Loss, T. Walczyk, and T. Prohaska. Atomic weights of the elements 2013 (iupac technical report). *Pure and Applied Chemistry*, 88(3):265–291, 2016.

[10] D.A Steck. Rubidium 87 d line data. *https://steck.us/alkalidata/*.

[11] A. Ashkin. Trapping of atoms by resonance radiation pressure. *Phys. Rev. Lett.*, 40:729, 1978.

[12] C. Doppler. *Über das farbige Licht der Doppelsterne und einiger anderer Gestirne des Himmels*. Abhandlungen der k

[13] W.D. Phillips. Nobel lecture: Laser cooling and trapping of neutral atoms. *Rev. Mod. Phys.*, 70(3):721–741, 1998.

[14] J. Dalibard and C. Cohen-Tannoudji. Laser cooling below the doppler limit by polarization gradients: simple theoretical models. *Journal of the Optical Society of America B*, 6.11:2023, 1989.

[15] S. Minniberger, F. Diorico, S. Haslinger, Ch. Hufnagel, N. Lippok Ch. Novotny, J. Majer, Ch Koller, S. Schneider, and J. Schmiedmayer. Magnetic conveyor belt transport of ultracold atoms to a superconducting atomchip. *Applied Physics B*, 116(4):1017–1021, 2014.

[16] url: https://www.mpq.mpg.de/5020878/0522a_bec.pdf.

[17] H. K. Onnes. On the sudden change in the rate at which the resistance of mercury disappears. *Communications from the Physical Laboratory of the University of Leiden, 124c. English translation in KNAW Proceedings*, 14II:818–821, 1912.

[18] C.M. Rey and A.P. Malozemoff. "fundamentals of superconductivity" in superconductors in the power grid. *Elsevier*, pages 29–73, 2015.

[19] R. Flükiger. Overview of superconductivity and challenges in applications. *Reviews of Accelerator Science and Technology*, pages 1–23, 2012.

[20] H. Rogalla and P. H. Kes. *100 Years of Superconductivity*. Taylor and Francis, 2012.

[21] url:http://www.open.edu/openlearn/science-maths-technology/engineering-and-technology/engineering/superconductivity/content-section-3.1.

[22] F. London and H. London. The electromagnetic equations of the supraconductor. *Proceedings of the Royal Society of London A: Mathematical, Physical and Engineering Sciences*, 149.866:71–88, 1935.

[23] V.L. Ginzburg and L.D. Landau. On the theory of superconductivity. *Zh. Eksp. Teor. Fiz.*, 20.1064, 1950.

[24] Superconductivity i (introduction to superconductivity) manuscript of the lectures for ss2006, url: http://www.pit.physik.uni-tuebingen.de/pit-ii/en/index.html.

[25] C. Kittel. *Introduction to solid state physics*. New York: John Wiley and Sons, 1986.

[26] F. Diorico. *Novel Atomchip Technologies with Superconductors*. PhD thesis, Atominsisut Der Österreichsichen Universitäten, TU Wien, Vienna, Austria, 2016.

[27] S. Minniberger. *Ultracold atoms on superconducting atomchips*. PhD thesis, Atominsisut Der Österreichsichen Universitäten, TU Wien, Vienna, Austria, 2017.

[28] R. Amsüss. Development of a source of ultracold atoms for cryogenic environments. Master's thesis, Atominsisut Der Österreichsichen Universitäten, TU Wien, Vienna, Austria, 2008.

[29] B. Gerstenecker. Tailoring trap current distributions in superconducting atomchips. Master's thesis, Atominsisut Der Österreichsichen Universitäten, TU Wien, Vienna, Austria, 2017.

[30] S. Haslinger. *Cold Atoms in a Cryogenic Environment*. PhD thesis, Atominsisut Der Österreichsichen Universitäten, TU Wien, Vienna, Austria, 2011.

[31] T. Weigner. Superconducting atomchips. Master's thesis, Atominsisut Der Österreichsichen Universitäten, TU Wien, Vienna, Austria, 2018.

[32] T. Pyragius. Developing and building an absorption imaging system for ultracold atoms. *arXiv:1209.3408 [physics.ins-det]*, 2012.

[33] M.Trimmel. Design and construction of an absorption imaging system for bose einstein condensate. Master's thesis, Atominsisut Der Österreichsichen Universitäten, TU Wien, Vienna, Austria, 2011.

[34] D. A. Smith, S. Aigner, S. Hofferberth, M. Gring, M. Andersson, S. Wildermuth, P. Krüger, S. Schneider, T. Schumm, and J. Schmiedmayer. Absorption imaging of ultracold atoms on atom chips. *Optics Express*, 19(9):8471–8485, 2011.

[35] D.M. Brink and C.V. Sukumar. Majorana spin-flip transitions in a magnetic trap. *Physical Review A*, 74:035401, 2006.

[36] O. Morizot, C. L. Garrido Alzar, P.-E. Pottie, V. Lorent, and H. Perrin. Trapping and cooling of rf-dressed atoms in a quadrupole magnetic field. *Journal of Physics B: Atomic, Molecular and Optical Physics*, 40:4013–4022, 2007.

[37] R. Salem. *Bose-Einstein Condensate on the Atom Chip*. PhD thesis, Ben-Gurion University of the Negev, 2010.

[38] B. Kasch, H. Hattermann, D. Cano, T. E. Judd, S. Scheel, C. Zimmermann, R. Kleiner, D. Koelle, and J. Fortágh. Cold atoms near superconductors: atomic spin coherence beyond the johnson noise limit. *New Journal of Physics*, 12, 2010.

[39] C. Roux, A. Emmert, A. Lupascu, T. Nirrengarten, G. Nogues, M. Brune, J.-M. Raimond, and S. Haroche. Bose-einstein condensation on a superconducting atom chip. *EPL (Europhysics Letters)*, 81(5):56004, 2008.

[40] H. Imai, K. Inaba, H. Tanji-Suzuki, M. Yamashita, and T. Mukai. Bose–einstein condensate on a persistent-supercurrent atom chip. *Appl. Phys. B*, 116:821–829, 2014.

[41] url: https://commons.wikimedia.org/wiki/file:magnetisation_and_superconductors.png.

[42] A. Patel. *Pulsed Field Magnetization of Composite Superconducting Bulks for Magnetic Bearing Applications*. PhD thesis, Department of Materials Science and Metallurgy, University of Cambridge, 2013.

[43] R.G. Mints and A.L. Rakhmanov. Critical state stability in type-ii superconductors and superconducting-normal-metal composites. *Rev. Mod. Phys.*, 53:551–592, 1981.

[44] P.W. Anderson. Theory of flux creep in hard superconductors. *Phys. Rev. Lett.*, 9:309, 1962.

[45] P. W. Anderson and Y. B. Kim. Hard superconductivity: Theory of the motion of abrikosov flux lines. *Rev. Mod. Phys.*, 36, 1964.

[46] W. Bucke and R. Kleiner. *Superconductivity: Fundamentals and Applications*. WILEY-VCH Verlag GmbH Co, 2004.

[47] E.H. Brandt and M. Indenbom. Type-ii-superconductor strip with current in a perpendicular magnetic field. *Phys. Rev. B*, 48(17), 1993.

[48] V. Dikovsky, V. Sokolovsky, B. Zhang, C. Henkel, and R. Folman. Superconducting atom chips: advantages and challenges. *The European Physical Journal D*, 51:247–259, 2009.

[49] W.J. Riley. *Handbook of Frequency Stability Analysis*. Hamilton Technical Services, Beaufort, SC 29907 USA, 2007.

[50] D.W. Allan. Should the classical variance be used as a basic measure in standards metrology. *IEEE Trans. Instrum. Meas.*, IM-36:646–654, 1987.

[51] D.W. Allan. Conversion of frequency stability measures from the time-domain to the frequency-domain, vice-versa and power-law spectral densities. 26 January 2012.

[52] D.W. Allan. Allan variance. *Allan's TIME*.

[53] D.W. Allan. The statistics of atomic frequency standards. *Proc. IEEE*, 54(2):221–230, Feb. 1966.